Computers in Biology and Medicine 195 (2025) 110379

Contents lists available at ScienceDirect

Computers in Biology and Medicine

journal homepage: www.elsevier.com/locate/compbiomed

Automated image analysis software for the study and quantification of retinal glial cells

Miguel A. Sánchez-Puebla [a,1], Lidia Sánchez-Puebla [b,c,d,1], Ana Granados [a,1], Valentín Moreno [a], Inés López-Cuenca [b,c,e], Ana I. Ramírez [b,c,e], José M. Ramírez [b,c,d], Juan Llorens [a,*]

[a] Carlos III University of Madrid, Computer Science Department, 28911, Leganés, Spain
[b] Ramon Castroviejo Institute for Ophthalmic Research, Complutense University of Madrid, 28040, Madrid, Spain
[c] Health Research Institute of the Hospital Clínico San Carlos (IdISSC), 28040, Madrid, Spain
[d] Department of Immunology, Ophthalmology and ENT, School of Medicine, Complutense University of Madrid, 28040, Madrid, Spain
[e] Department of Immunology, Ophthalmology and ENT, Faculty of Optics and Optometry, Complutense University of Madrid, 28040, Madrid, Spain

ARTICLE INFO

Keywords:
Automatic image analysis
Retinal microglia
Cell quantification
Soma characterization
Skeletonization computation
Arborization area calculation

ABSTRACT

Microglia, the resident macrophages of the central nervous system, play a key role in immune surveillance, homeostasis, and neurodegenerative processes. Manual microglia analysis is time-consuming and prone to subjective bias, while most automated methods focus on quantification rather than characterization. Additionally, few tools are specifically designed for retinal microglia analysis. In this study, we present a novel automated image analysis software for microglia evaluation, integrating soma detection, quantification, characterization, skeletonization, and arborization measurement-the latter two being automated for the first time. The software was validated against expert manual annotations on 1,702 images fluorescence microscopy images of murine retinal tissue (24,559 cells), assessing its performance across both high- and low-quality images to evaluate its robustness in large-scale datasets. Our software processes images over 1,000 times faster than manual methods while maintaining high accuracy. It successfully analyzes low-quality images, though excluding them improves performance. The algorithm's ability to extract morphological features with high reproducibility enhances dataset usability, optimizing sample use and reducing animal sacrifices. This is the first tool to automate microglial skeletonization and arborization measurement, establishing a new standard for retinal microglia analysis. Its efficiency, scalability, and ability to handle varied image quality make it a valuable resource for large-scale studies. Future applications will focus on leveraging the reference values established in this study to advance neurodegenerative disease analysis, marking a significant step toward more sophisticated microglial research.

1. Introduction

Microglia, the phagocytic cells of the central nervous system, are crucial for clearing cellular debris, participating in all inflammatory and neurodegenerative processes, maintaining tissue homeostasis, and promoting normal brain development under typical conditions. Notably, this cell type constitutes 15%–20% of the total glial cell population in human adult brain [1].

In physiological conditions, microglial cells have a small soma that can take on triangular, rounded, or oval shapes, with cell processes that have a conical morphology, thicker near the cell body and thinning outward [2]. From the primary processes, secondary and tertiary processes originate, giving rise to a ramified form [3]. Microglia are uniformly distributed throughout the nervous tissue, resembling a mosaic pattern, with limited interaction with neighboring cells [4,5]. However, microglial cells present remarkable morphological plasticity that varies depending on the cellular developmental stage, the state of the nervous system, and the specific function they are performing [6].

Retinal microglia cells are uniformly distributed throughout the retina and can be found in various layers, exhibiting distinct morphologies depending on their location and activation state. Highly ramified cells are observed in the plexiform layers, while in the nuclear layers they usually present a more compact shape [7,8]. Under physiological conditions, microglial cells are in a quiescent state. This state is characterized by a ramified morphology in the outer plexiform layer and

* Corresponding author.
E-mail address: llorens@inf.uc3m.es (J. Llorens).
[1] These authors contributed equally to this work.

https://doi.org/10.1016/j.compbiomed.2025.110379
Received 22 November 2024; Received in revised form 24 April 2025; Accepted 10 May 2025
Available online 27 June 2025

inner plexiform layer. In this state, microglia express low levels of co-stimulatory molecules and display minimal phagocytic activity [9–12]. Upon activation in response to damage, microglia undergo morphological changes [11,12], initially adopting a hyper-ramified form with increased complexity in secondary extensions, responding to changes in neuronal activity [13]. In an advanced state of activation, microglia transition to a reactive state, with thicker and retracted processes, and an enlarged soma. They release factors like M-CSF and GM-CSF, and pro-inflammatory cytokines [14,15], and they may migrate toward the site of injury to interact with damaged neurons and clear away dead cell debris [16]. In an advanced reactive state, microglia acquire an amoeboid phenotype, characterized by a round morphology with few or no processes, often associated with phagocytic functions [15]. Finally, in a senescent or dystrophic state, microglia is characterized by cytoplasmic fragmentation and cell death, and the release of higher pro-inflammatory cytokines, generating chronic inflammatory mediators associated with neuroinflammation [17].

Neurodegenerative diseases involve neuroinflammation, where microglia play a key role [15]. Conditions like Alzheimer's disease [18–20], Parkinson's disease [21,22], amyotrophic lateral sclerosis [23,24], Friedrich's ataxia [25], and chronic glaucoma [26–28] are linked to protein aggregates and neuronal degeneration. Activated microglia release pro-inflammatory cytokines, propagating and worsening neuroinflammation, triggering neuronal degeneration, and impairing brain function [15].

Considering the crucial role of microglia in neuroinflammation and neurodegenerative diseases, recent advances in technology have become instrumental. Traditionally, observations and counting, as well as characterization, were done manually. This manual analysis, which involves marking pixels to calculate the area of arborization of each individual cell, is an excessively time-consuming process, susceptible to human error. Besides, manually measuring the total cell perimeter accurately becomes almost unfeasible. Another drawback of manual characterization is the inter-observer variability, as the morphological boundaries between one stage and another can be very subtle [29]. The criteria used by medical experts in manual analysis are very subjective and effective blinding is not always possible when studying disease and injury models with distinctive histopathological features. Subjectivity becomes an even greater issue if researchers wish to include in their analysis the hyper-ramified morphotype, which is difficult to identify/separate from homeostatic and reactive morphotypes [30,31].

To address these challenges, different automated methods for quantifying microglial cells [32–34] and studying their morphology using machine learning [35–37] have emerged as powerful tools in biomedical research. Despite the advancement these algorithms represent, the former methods solely focus on counting microglial cells and do not include the analysis of their morphology, while the latter automatically classify images of retinal microglial cells into several morphotypes but provides limited insights into their characteristics. Besides, these algorithms focus on the analysis of microglia from different parts of the central nervous system, and few are suitable for use in the retina [38]. Therefore, more comprehensive automated retinal image analyses are needed.

The aim of our paper is to present a new automated image analysis software specifically designed to detect, quantify, and characterize somas, perform their skeletonization, and accurately calculate the arborization area of these cells in retinal tissue. It should be highlighted that our software is the result of combining expertise in software engineering/computer science with the knowledge of neuro-ophthalmologists.

2. Materials and methods

2.1. Image acquisition

Retina samples were obtained from C57BL/6J laboratory mice (Charles Rivers Laboratory, Barcelona, Spain). Samples were then stained for microglia using ionized calcium binding adaptor molecule 1 (Iba-1, the most used marker of microglia; Wako, rabbit anti-Iba1).

Each retina was divided into 4 areas (superior, inferior, nasal, and temporal), and each area was further subdivided into three sectors (peripapillary, intermediate, and peripheral relative to the optic disc), and photographed at a 20x magnification, resulting in a total of 36 photographs for each whole-mount retina. Images were acquired in the outer plexiform layer and inner plexiform layer of each retina, resulting in a total of 1702 images.

For image acquisition, a Zeiss Axioplan 2 fluorescence microscope equipped with the Axio Cam 503 Mono digital camera was used. The microscope was equipped with a Zeiss 64 filter set for Alexa Fluor 594, enabling the visualization of the emission spectrum of the fluorochromes used in the secondary antibodies (568 nm).

2.2. System description

Our software for counting and analyzing retinal microglial cells has powerful capabilities, including soma detection, quantification, and characterization, along with skeletonization and precise calculation of arborization areas. The following subsections explain the details of the algorithms implemented in our system. Besides, for clarity, Fig. 1 shows a flowchart summarizing all the information presented in the following subsections. For additional details, refer to Appendix B, which presents sequence diagrams for further description of the main steps.

Before diving into the core of the system description, we find it helpful to clarify some biological concepts to ensure accessibility for readers from diverse backgrounds. According to [39], morphologically, the soma of a neuron represents the central, typically expanded or bulbous part of the cell. It stands in contrast to the slender, elongated neuronal processes, namely the dendrites and the axon, that extend outward from it. The shape and size of the soma can vary considerably across different neuronal types, ranging from spherical and pyramidal to stellate or irregular forms. It constitutes the main structural component from which all neuronal appendages originate. While these terms are traditionally associated with neurons, they are also used to describe analogous morphological structures in other cell types, such as microglia, which are the focus of this study.

2.2.1. Image preprocessing

Prior to a detailed explanation of the image processing [40], we provide an overview of relevant concepts to ensure clarity and inclusivity for a broader audience. In the context of soma image processing, binarization refers to the process of converting a grayscale image, where each pixel has an intensity value, into a binary image. In a binary image, each pixel can take on only one of two possible values, typically representing the foreground (soma) and the background. The primary goal of binarization is to isolate the somas of interest from the surrounding tissue or noise, thereby simplifying subsequent analyses such as size measurement, shape analysis, or counting.

Thresholding [40] is a fundamental technique used to achieve binarization. It involves selecting one or more intensity values, known as thresholds, to classify pixels into foreground and background categories. Pixels with intensity values above (or below, depending on the convention) the threshold are assigned one binary value (e.g., white or 1), while the remaining pixels are assigned the other binary value (e.g., black or 0). The choice of threshold value is crucial for the accurate segmentation of somas.

Building on these concepts, our software preprocesses each image through a series of steps, beginning with grayscale conversion (step 1 of Fig. 1), applying Gaussian blur filtering [41] (step 2 of Fig. 2) with a 3×3 kernel and standard deviation given as zeros, to obtain a smoother and less noisy image, and then segmenting the images by binarization [41] (step 3 of Fig. 2). This prevents machine crashes caused by images with high levels of noise and simplifies their analysis.

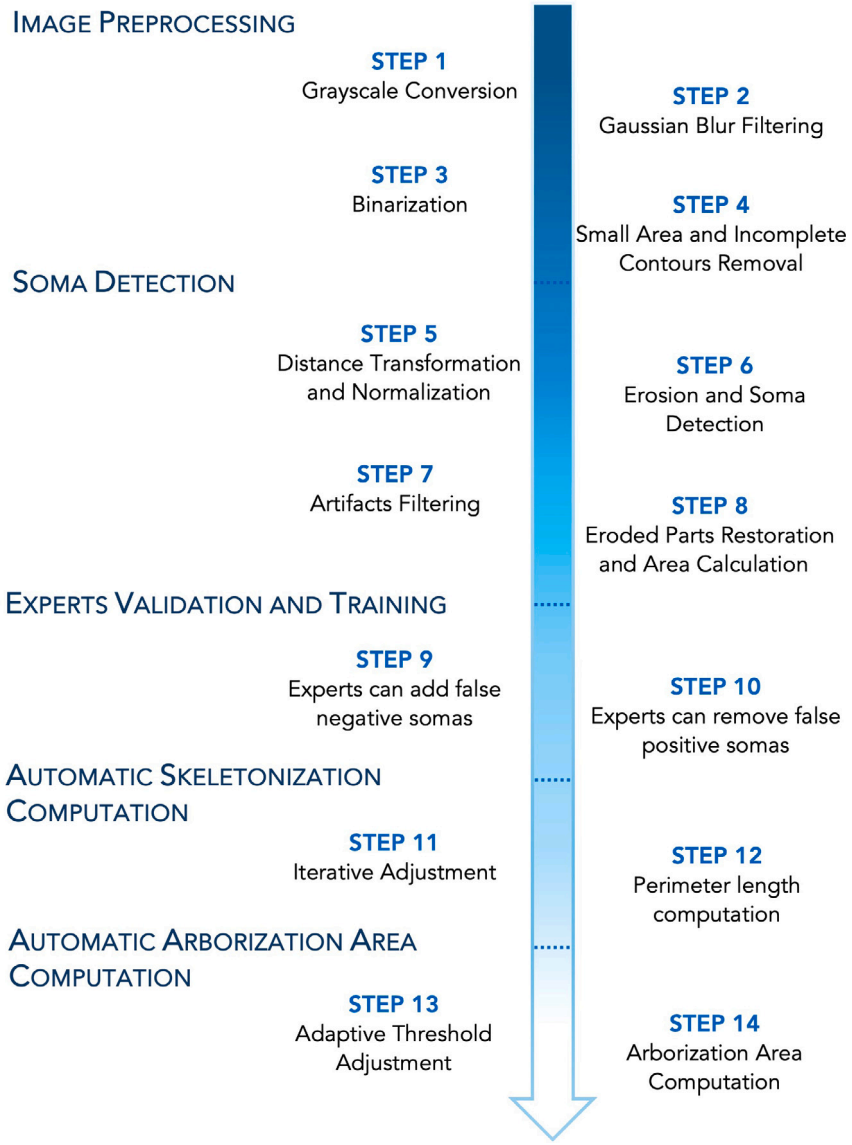

Fig. 1. System Flowchart. First, the image undergoes preprocessing. Next, soma detection is performed, allowing the user to add or remove somas if needed. Then, the skeletonization results are computed and presented to the user. Finally, the arborization area computations are displayed.

The segmentation by binarization (step 3 of Fig. 2) starts by setting the optimal threshold for binarizing each image [42]. The threshold is calculated individually, based on the following idea: as the binarization threshold increases, somas become more isolated, but some may become unrecognizable due to the decrease in the area enclosed by the contour. The optimal binarization threshold is the one that preserves the somas while decreasing the number of detected contours. Particularly, the specific condition satisfied by the threshold that has been chosen as the optimal is that the first derivative of the number of contours with respect to the gray-level-intensity is negative while the second derivative is zero or positive.

Finally (step 4 of Fig. 2), our algorithm eliminates all contours with an area smaller than 20 μm^2 (this parameter can be adjusted into the tool with values provided by the medical experts), as no soma has its area below this value [36,43]. Additionally, if the minimum bounding rectangle for any soma contour touches the image borders, it is removed because it is incomplete. This filtering step significantly reduces the number of contours from potentially hundreds of thousands to just a few hundred reducing the computation time.

2.2.2. *Soma detection*

After preprocessing the image (step 1 to step 4), the soma detection phase involves applying several image processing techniques. Firstly, a Region of Interest (ROI) and a mask are created per each remaining contour. Then, a simple Euclidian distance transformation is applied and normalization is performed in a range [0,1] (step 5), to each ROI because cell processes (extensions of the cell that reach out from the main body) are located at the periphery, while the soma (main body) is more rounded and closer to the center of mass (see Fig. 3A). It should be highlighted that in physiological conditions, microglial cells have a small soma that can take on triangular, rounded, or oval shapes, with cell processes that have a conical morphology, thicker near the soma and thinning outward [2]. From the primary processes, secondary and tertiary processes originate, giving rise to a ramified form [3]. Microglia are uniformly distributed throughout the nervous tissue, with limited interaction with neighboring cells [4,5], however, microglia present remarkable morphological plasticity that varies depending on the developmental stage, nervous system state, etcetera [6].

Secondly (step 6), erosion is applied in several consecutive steps using a 3×3 kernel to separate cell processes from their respective

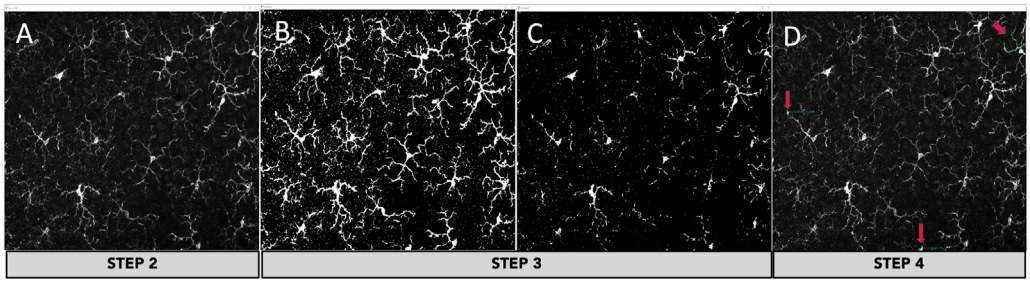

Fig. 2. Image processing steps. (A) Original grayscale image after Gaussian blur filtering (Step 2). (B) Binarized image highlighting microglial structures (Step 3). (C) Image after small area and incomplete contour removal, refining the segmentation (Step 3). (D) Examples of removed contours with area smaller than 20 μm^2 or incomplete soma (Step 4).

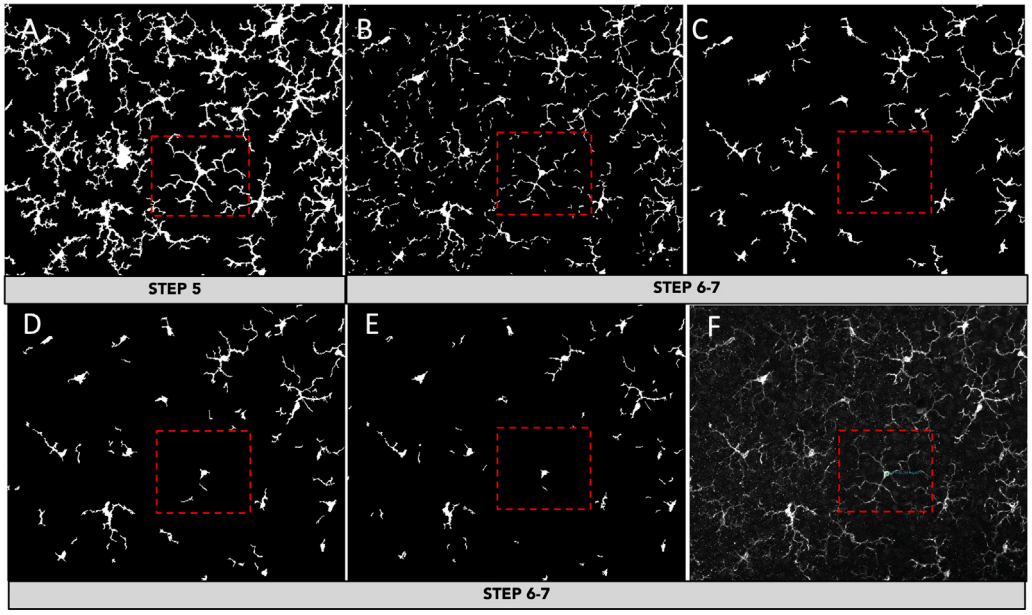

Fig. 3. Progressive refinement of microglial structure segmentation. (A) Distance transformation and normalization highlighting microglial processes (Step 5). (B-E) Iterative filtering of soma and process contours through erosion and soma detection and artifact removal (Steps 6-7). (F) Overlay of the final segmentation on the original grayscale image, demonstrating the accuracy of detected structures. The red dashed boxes highlight a representative region of interest throughout the process.

somas [41]. It must be pointed out that other kernel sizes (5×5, 7×7) produce poorer soma detection results. The erosion process increases the number of shapes because a soma with cell processes leads to several contours [15,26]. During the erosion process, processes are separated from their somas (see Fig. 3B–F).

Soma identification relies on both the contour with the largest area and the lowest circularity index, considering the circularity calculated using the standard non-dimensional formula $(perimeter \times perimeter)/area$ [44]. The area of all the detected shapes is calculated by applying the Green's theorem [45] (step 7). Since the images captured by the microscope used are consistently of the same size, we can determine the $pixel - to - \mu m^2$ conversion ratio (1 pixel = 0.227 μm, according to the data provided by the microscope documentation), which ensures accurate measurement of detected shapes' areas.

Additionally, this process includes an artifact filtering step, which involves automatically adding or removing contours identified as somas or processes by matching contours through Hu moments [46] collected and stored on previously analyzed images confirmed by experts in previous processing images.

The loop including the erosion process and soma detection (Step 6) and artifact filtering (step 7) is stopped when there is no soma identified in the ROI, or the position of the center of mass (CM) of each soma included in the ROI varies less than p pixels (typically 10 pixels for an image resolution of 1936×1460), while the soma area remains stable across consecutive iterations (see Fig. 4A–C).

Once the somas are successfully detected, any previously eroded parts are restored to their original state before erosion, ensuring the accurate recovery of cells' true size. This ensures the computation of real somas' areas (Step 8 of Fig. 4D). This computation depends on these parameters:

- The ROI containing a single soma may require several thresholds to ensure that the overall area of the soma is well captured because non-uniform variations in intensity may result, for example, due to variation during image acquisition conditions. This is a key feature since current fully automated approaches use only one user defined threshold for the segmentation process [47].
- The value used for the morphological opening and closing operations also depends on the threshold: the higher the threshold, the smaller the closing value should be, resulting in preserving the original shape of the soma.
- The circularity index [44] to differentiate somas from processes. Processes feature a higher circularity index.

However, variation in image acquisition condition could occur that will produce non-uniform variation in intensity in a tissue image, and it is worth highlighting that even if the overall process is performed automatically and the optimal threshold is calculated automatically, to empower human experts to select the most suitable binarization threshold for a specific part of the image, we have incorporated a

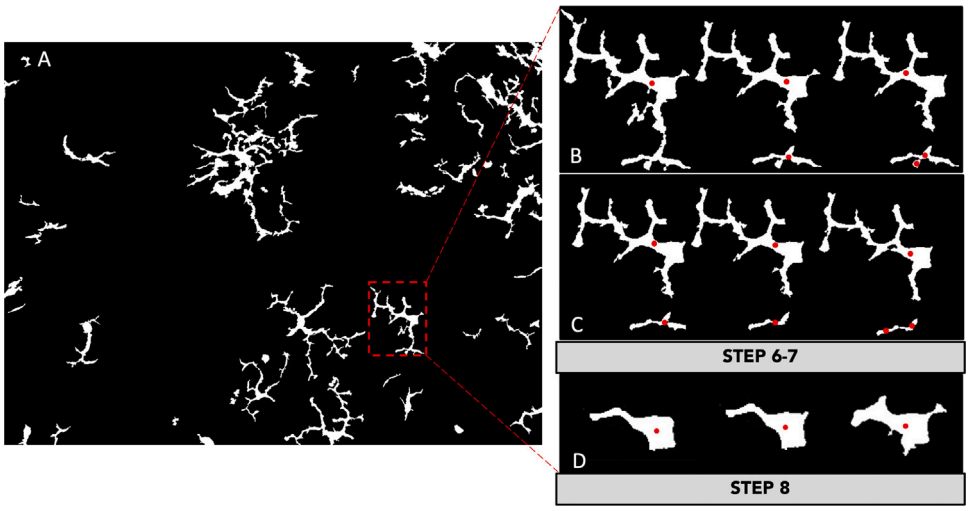

Fig. 4. (A, B, C) Detailed erosion to separate cell processes from somas (Step 6) and artifact filtering (Step 7) . The red dot corresponds to the center of mass. (D) Restoration of the eroded part (Step 8).

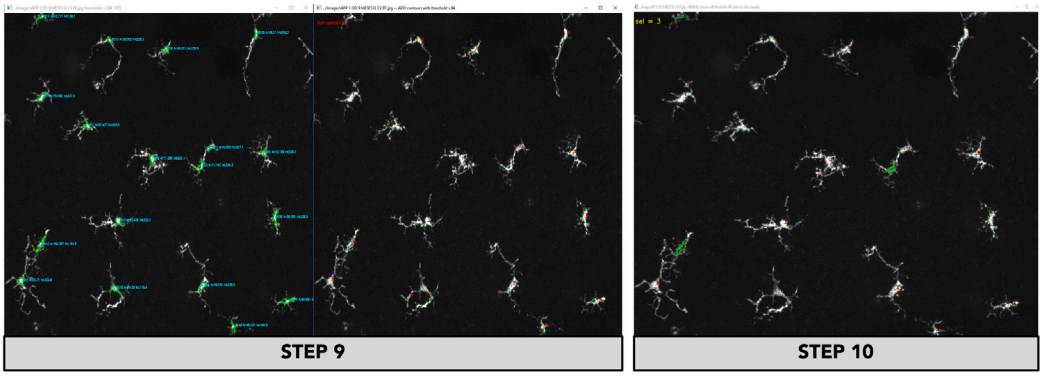

Fig. 5. Expert validation of soma detection. After automated analysis, the tool presents two windows for expert to review the results. In Step 9, experts can add missed somas by adding missed somas -not required in this example-, while in Step 10, they could remove false detections (highlighted in green) and confirm correctly identified somas, ensuring accurate detection.

track-bar into our tool (Fig. A.2, see Appendix A). This interactive functionality allows medical experts to dynamically adjust the threshold for each image, enabling fine-tuning to determine the optimal value based on their expertise and judgment. Additionally, it facilitates the standardization of expert criteria when deemed necessary.

After the automated image analysis, our tool generates two windows for expert review. In Step 9, medical experts can add any somas that the algorithm may have missed (false negatives, FN). In Step 10, they can remove incorrectly detected somas (false positives, FP) and validate correctly identified somas (true positives, TP). The tool will use the added and removed contours to learn, when processing further images, at step 7. This expert intervention ensures the accuracy and reliability of soma detection (see Fig. 5).

FP occur due to the identification of biological markers and waste as somas, as they share similar morphological features with true somas. FN arise when somas are intuitively recognized by experts as present in the image, even if they lack the typical morphological features of a soma. Our tool records TP, FP and FN, compares the stored contours and predicts new results by matching contours through Hu moments [46]. Besides, these windows allow medical experts to unify measurement criteria and serve as an enabler for conducting training sessions.

2.2.3. Skeletonization

Once soma contours are identified in an image, automatic skeletonization can be performed, a process that simplifies the cell structures into line-like representations of their branches. Our cell skeletonization algorithm closely resembles our soma detection algorithm, but it involves a more sophisticated approach to handling intensity binarization thresholds, because it considers the overlapping regions between adjacent contours. The correlation with soma contours identified in previous steps is performed through the center of mass. Each skeletonization contour is represented with a red identification number located at the center of mass position in Fig. 6. Also, holes inside a skeletonization contours are detected.

The skeletonization process iterates by progressively lowering the threshold for contour identification, starting from the threshold set by the soma detection algorithm (Fig. 6A–F). The loop ends when the contour of one specific soma starts to overlap with any contour of the rest of the somas (Fig. 6G–H). Then, the said threshold is locked, and the exploration of possible thresholds continues only for the rest of the image. This iterative process repeats until the entire image is processed completely. Finally, the perimeter length of each contour is calculated by counting the number of pixels that belong to the skeletonization contour (step 12 of Fig. 6-I). Notably, regions at the image boundaries are excluded, as their areas are not considered representative for medical experts.

It is worth noting that skeletonization measures cannot be computed manually with an acceptable accuracy in a reasonable period of time, which constitutes a pivotal strength of our tool.

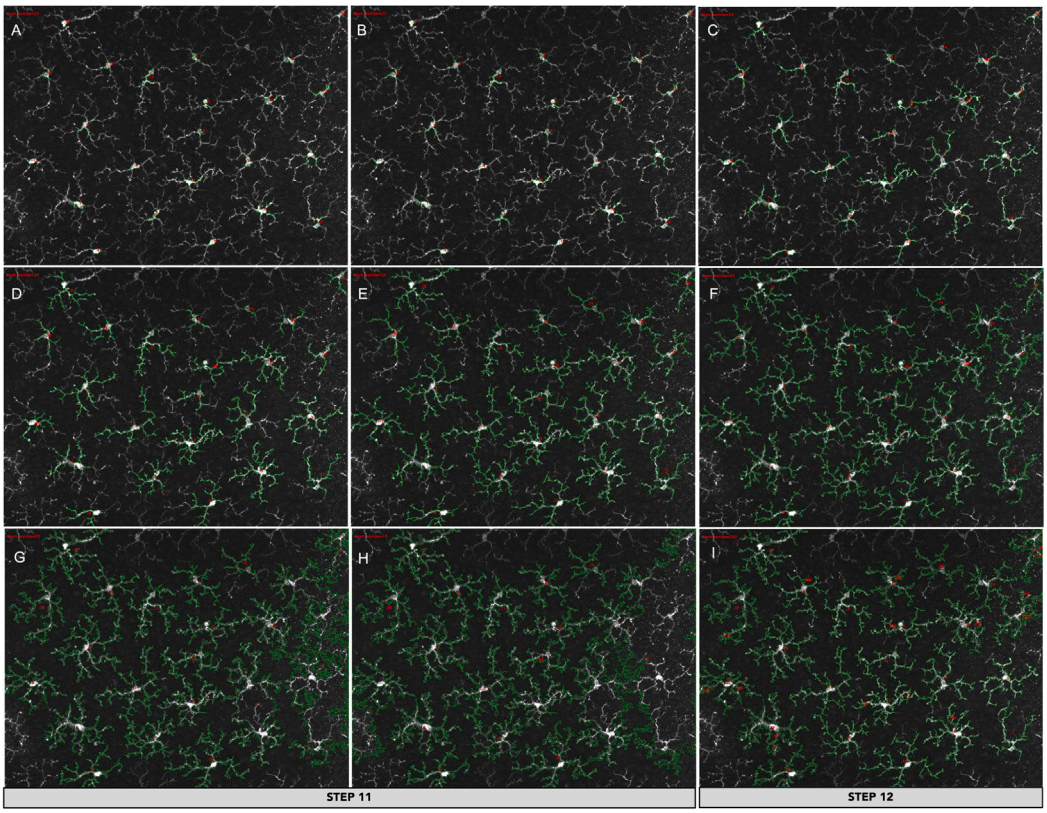

Fig. 6. (A–H) Step 11: iterative skeletonization adjustment starting from high values (A) the threshold is decreased until the skeletonization is computed for all somas (I). At each iteration, the threshold is determined per each soma and locked when overlaps with other contours (G–H). Each locked skeletonization contour is frozen and excluded in the next iteration. (I) Step 12: final perimeter length computation.

2.2.4. Arborization area

Our arborization area algorithm (step 13 of Fig. 7) follows the same principle than our skeletonization algorithm, considering the overlapping regions between adjacent cell arborization areas, locking thresholds when an overlap occurs, and exploring possible thresholds only for the remaining cells, until the entire image is processed completely. Similarly, arborization contours reaching the limits of the image are locked and rejected as their areas are not representative. Finally, the arborization area (step 14 of Fig. 7) is provided by the convex Hull contour [48] corresponding to the locked threshold, which defines the boundary covering the cell's branches.

2.2.5. Performance of microglia processing and segmentation workflow

Fig. 8 shows the performance of our soma detection capability, skeletonization and arborization area algorithm when applied to several images ranging from low to high levels of complexity based on noise levels and image quality. It can be seen that our tool effectively handles all the images, demonstrating its robustness and versatility in different scenarios.

2.2.6. User interface

Additional details on the tool's execution and user interface are provided in Appendix A.

3. Results

A total of 1702 images were analyzed using our automated image processing tool. The processing of these images took approximately 8 h in a laptop with 11th Gen Intel(R) Core(TM) i5-1145G7 @ 2.60 GHz 16 GB RAM and GPU Intel Iris Xe Graphics 8 GB, during which the tool marked the soma, determined the area of cell branching or arborization, performed skeletonization to measure the total cell perimeter, and generated the corresponding Excel tables. These tables included all the crucial information as assessed by medical experts and the key data required for facilitating the tool's automatic evaluation.

3.1. Algorithm effectiveness assessment

To evaluate the effectiveness of the proposed algorithm, typical performance metrics such as precision (P), recall (R) and F1-score (F1) have been calculated. In our experiments, for a set of 1702 images and 24,559 somas validated by medical experts with TP = 21,855; FP = 2025; FN = 679 the metrics obtained are:P = 0.92; R = 0.97 and F1 = 0.94 (see Table 1). With the complete set of 1702 images, the false positive (FP) rate is 8.25%, which includes low-quality images (20.92% of the dataset) affected by biological waste or marker artifacts from tissue processing that are typically discarded by experts due to the difficulty in manual measurements (see Fig. 9B).

Excluding low-quality images resulted in a significant performance improvement, with an increase in the P and F1-score to 0.97, while the FP rate decreased to 2.84%, and R remained stable at 0.97, demonstrating its high reliability under optimal conditions.

Fig. 9 shows examples illustrating the performance of the proposed image processing tool in analyzing microglial morphology under different image quality conditions. The tool effectively detects somas, traces microglial branching, and delineates arborization areas in both high- and low-quality images, demonstrating its reliability and adaptability.

The validation of our automated soma measurement tool was conducted by a medical expert with over two years of experience manually measuring somas from images obtained as described in Section 2.1, under the supervision of three additional experts. To assess the accuracy of the automated method, Fig. 10 compares manually measured soma areas with those computed by our algorithm. The observed variations can be attributed to differences in expert practices, such as contour

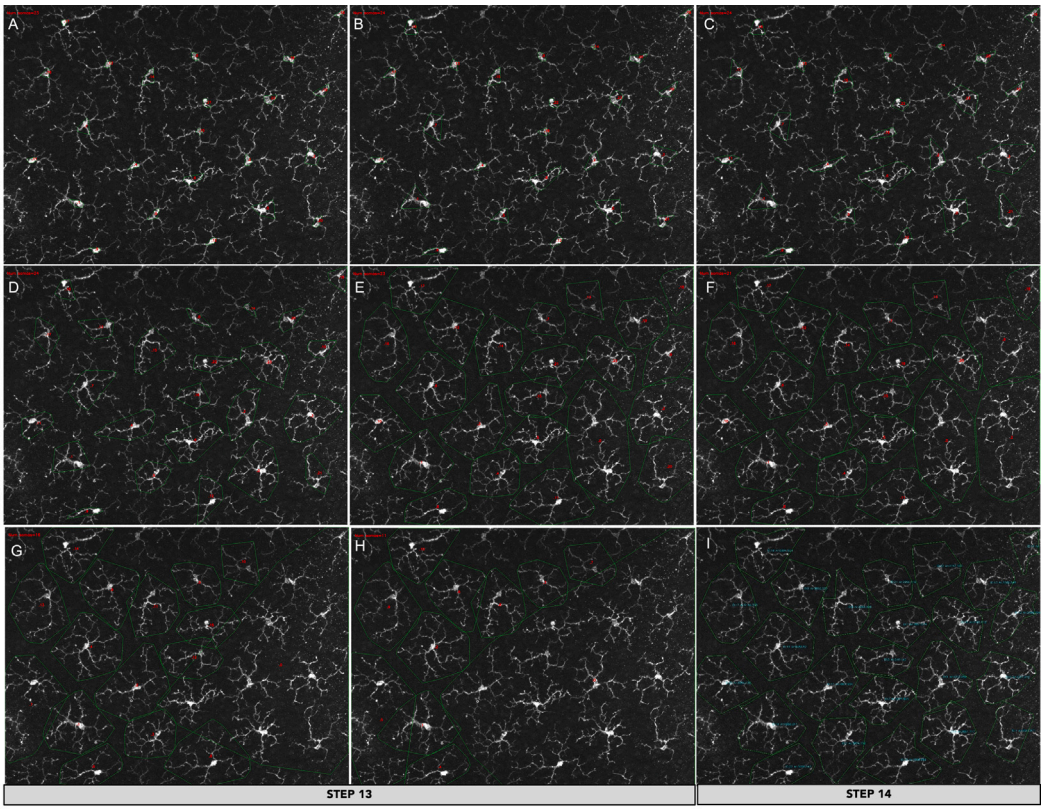

Fig. 7. (A–H) Step 13: Progressive identification of individual microglial cells and delineation of their arborization areas (green contours), illustrating the incremental refinement in soma and arborization detection with the adaptive threshold adjustment per Hull Contour. (I) Step 14: final arborization area computation.

Table 1
Performance metrics of the algorithm for soma detection using the full dataset (1702 images) and after removing low-quality images (1345 images).

Metric	Full set of Images (1,702 images)	After Removing Low-Quality Images (20.92%) (1,345 images)
Number of somas	24,559	19,466
True Positives (TP)	21,855 (88.99%)	18,369 (94.36%)
False Positives (FP)	2,025 (8.25%)	553 (2.84%)
False Negatives (FN)	679 (2.76%)	544 (2.79%)
Precision (P)	0.92	0.97
Recall (R)	0.97	0.97
F1-score (F1)	0.94	0.97

smoothing and the subjective determination of soma boundaries. Given that 1 pixel corresponds to 0.227 μm, expert criteria differences can account for approximately 40 pixels in a typical 50 μm^2 area, leading to an average discrepancy of 4.1% between computed and manual measurements. This level of variation highlights the challenges of inter-rater reproducibility in manual classification, particularly across different research groups [23,35]. The observed inconsistencies further emphasize the necessity of an automated approach, as our tool provides a standardized and reproducible method for soma measurement, reducing subjective bias and improving measurement reliability.

The mean absolute percentage error (MAPE) has been used to measure the percentage error between automatically computed and manually measured areas, both for somas' areas and arborization areas:

$$\mathrm{MAPE} = \frac{100\%}{N}\sum_{i=1}^{N}\frac{|m_i - c_i|}{m_i} \quad (1)$$

Where N is the number of values, m_i is the manually measured value by the experts and c_i is the computed value.

For arborization areas, regions touching the image boundaries (3967 arborization areas) have been discarded as these areas are not fully completed. In our experiments, the MAPE for soma areas was 9.12%, while the MAPE for arborization areas was 8.67% indicating a high level of accuracy. When lower-quality images were removed, the MAPE values improved to 8.85% for soma areas and 8.25% for arborization areas, demonstrating that excluding low-quality images enhances measurement accuracy.

No MAPE value has been calculated for skeletonization areas as there are no available results manually measured because their measurements are not affordable to perform manually with adequate precision for experts. Validation of skeletonization contours has been performed by manual inspection of the images provided by the tool. The total of the images has been inspected by 2 expert users. From this inspection, 97.3% of the contours have been confirmed by the experts. The main differences are found in the gaps that appear in the images and that separate pieces of the processes, although the expert easily fills them in and guesses that they must be parts of the same extension. These gaps are likely due to the acquisition process in the microscope or the migration of cells between the inner and outer plexiform layers (see Fig. 11).

Besides, the Bland-Altman analyses between the measurements made manually by an expert observer and the measurements provided by our tool, for the areas of somas with all images, showed limits of agreement of (−9.007 and 19.19) and the average for the soma area bias is 5.093 with a standard deviation of bias ±7.194. When calculating the same parameters after removing the low-quality images, the limits of agreement for the soma areas were (−16.28 and 12.69), with an average for the soma areas bias is −1.796 and a standard deviation of bias ±7.389 (Fig. 12A–B).

Similarly, the Bland-Altman analyses between the measurements made manually by an expert observer and those measurements provided by our tool, for the arborization areas with all images, showed

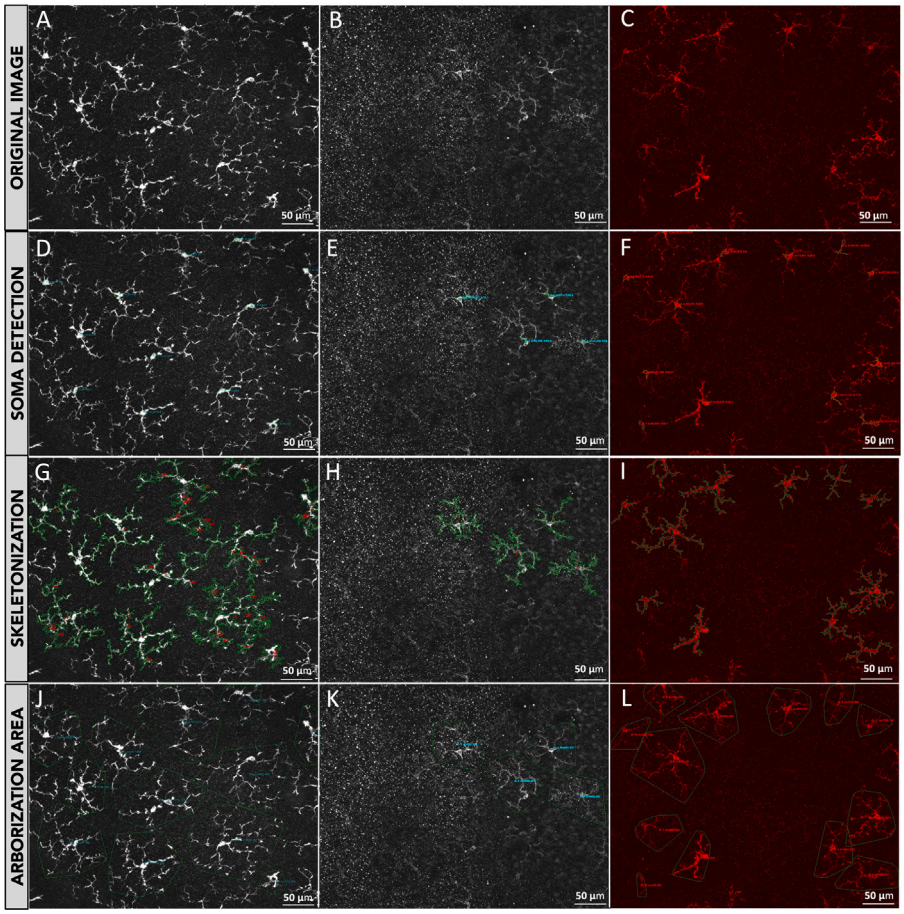

Fig. 8. Automated analysis of retinal microglia morphology under different conditions using the proposed image processing tool. (A–C) Original images of retinal microglia under varying conditions. (D–F) Soma detection using the automated tool, which accurately identifies and labels microglial somas (green), demonstrating its robustness across diverse imaging conditions. (G–I) Skeletonization performed by the tool, successfully extracting microglial branches (green) and highlighting critical branching points (red) to facilitate quantitative morphological analysis. (J–L) Arborization area detection, where the tool outlines individual microglial cells and their arborization (green), enabling quantitative assessments of morphological complexity. Images are arranged in increasing order of soma detection complexity, with (A) representing a simple case, (B) an intermediate level, and (C) a high degree of complexity.

limits of agreement of (−693.7 and 946.7) and an average for the arborization area bias is 126.5 with a standard deviation of ±418.5. By removing low-quality images, the limits of agreement were (−392.4 and 468.2) and the average for the arborization area bias is 37.88 and a standard deviation of ±219.6 (Fig. 12C–D).

Finally, the intraclass correlation coefficients (ICC) were calculated using a random effects and consistency model to compare manual and automatic measurements for both soma area and arborization area. Results were obtained for both single measures and average measures, considering all images and excluding low-quality images.

When calculated for the entire image set, the ICC for the soma area was 0.937 for single measures, with a 95% confidence interval (CI) of (0.930–0.943). For average measures, the ICC was 0.967, with a 95% CI of (0.964–0.971). After removing low-quality images, the ICC for the soma area was 0.961 for single measures, with a 95% confidence interval of (0.956–0.965), and 0.980 for average measures, with a 95% CI of (0.978–0.982).

For the arborization area, including the full set of images, the ICC for single measures was 0.945, with a 95% CI of (0.938–0.952). For average measures, the ICC was 0.972, with a 95% CI of (0.968–0.975). After removing low-quality images, the ICC for single measures increased to 0.988, with a 95% CI of (0.987–0.990), while for average measures, it reached 0.994, with a 95% CI of (0.993–0.995).

Lastly, the F-test for all ICCs yielded a p-value < 0.001, indicating statistical significance.

Table 2
Intraclass Correlation Coefficient (ICC) results under different conditions. CI: Confidence Interval. The F-test for all ICCs yielded a p-value < 0.001, indicating statistical significance.

Measurement area	Condition	Single measures		Average measures	
		ICC	95% CI	ICC	95% CI
Soma area	Full set of images	0.937	0.930 – 0.943	0.967	0.964 – 0.971
Soma area	Removing Low-quality images	0.961	0.956 – 0.965	0.980	0.978 – 0.982
Arborization area	Full set of images	0.945	0.938 – 0.952	0.972	0.968 – 0.975
Arborization area	Removing Low-quality images	0.988	0.987 – 0.990	0.994	0.993 – 0.995

All these results are summarized in Table 2.

3.2. Software's performance in pathological conditions

Although evaluating pathological conditions is not the main focus of this work, this subsection is included to provide a detailed assessment of our software's performance in such conditions, specifically in

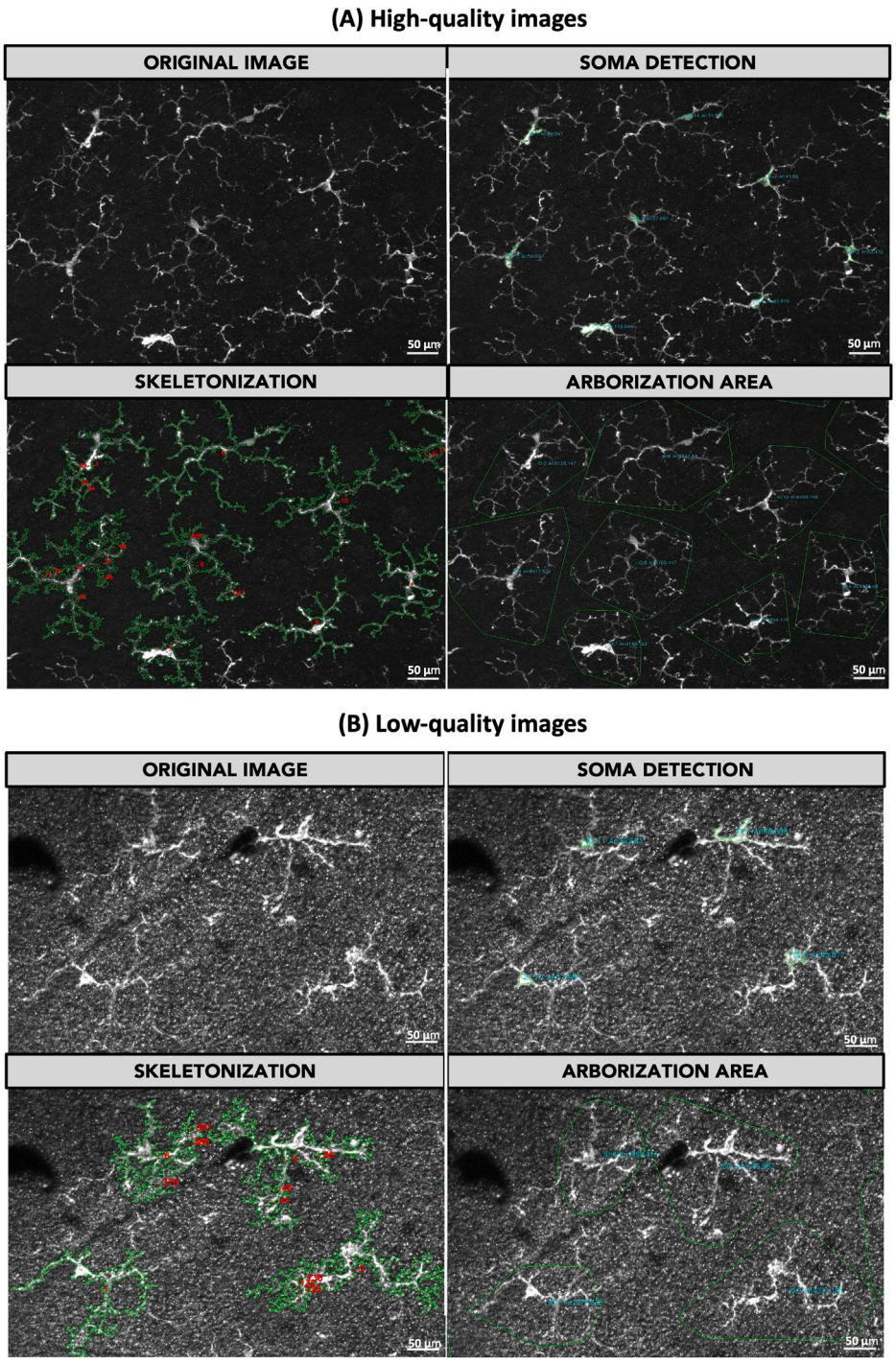

Fig. 9. Comparison of automated microglia analysis in high-quality (A) and low-quality (B) images using the proposed image processing tool. Each set includes the original image, soma detection (highlighted in green), skeletonization (showing microglial branches in green and critical branching points in red), and arborization area detection (with individual microglial cells outlined in green). Despite variations in image quality, the tool identifies key morphological features.

a murine model of Alzheimer's disease (AD). In light of this, while the primary validation was conducted on healthy retinal microglia, it is crucial to evaluate the tool's robustness in disease models, where microglial morphology undergoes significant alterations.

Fig. 13 compares the microglia from healthy control mice (C57BL/6J) and the AD model, demonstrating that our software successfully detects and quantifies somas, performs skeletonization, and measures arborization areas in both conditions. Notably, microglia in the Alzheimer's model exhibited increased complexity and reactivity, consistent with previous findings in neurodegeneration research.

These findings highlight the potential of our software for investigating microglial alterations in neurodegenerative diseases. While this study primarily establishes reference values under healthy conditions, future research will focus on applying the tool to disease models. Specifically, it will be used to quantify microglial responses to pathological stimuli, providing a standardized and automated approach for assessing morphological changes associated with neurodegeneration. To illustrate this capability, Fig. 14 shows the software's analysis of a murine model of AD. The images demonstrate the tool's ability to detect, segment, and quantify microglial morphology even in pathological

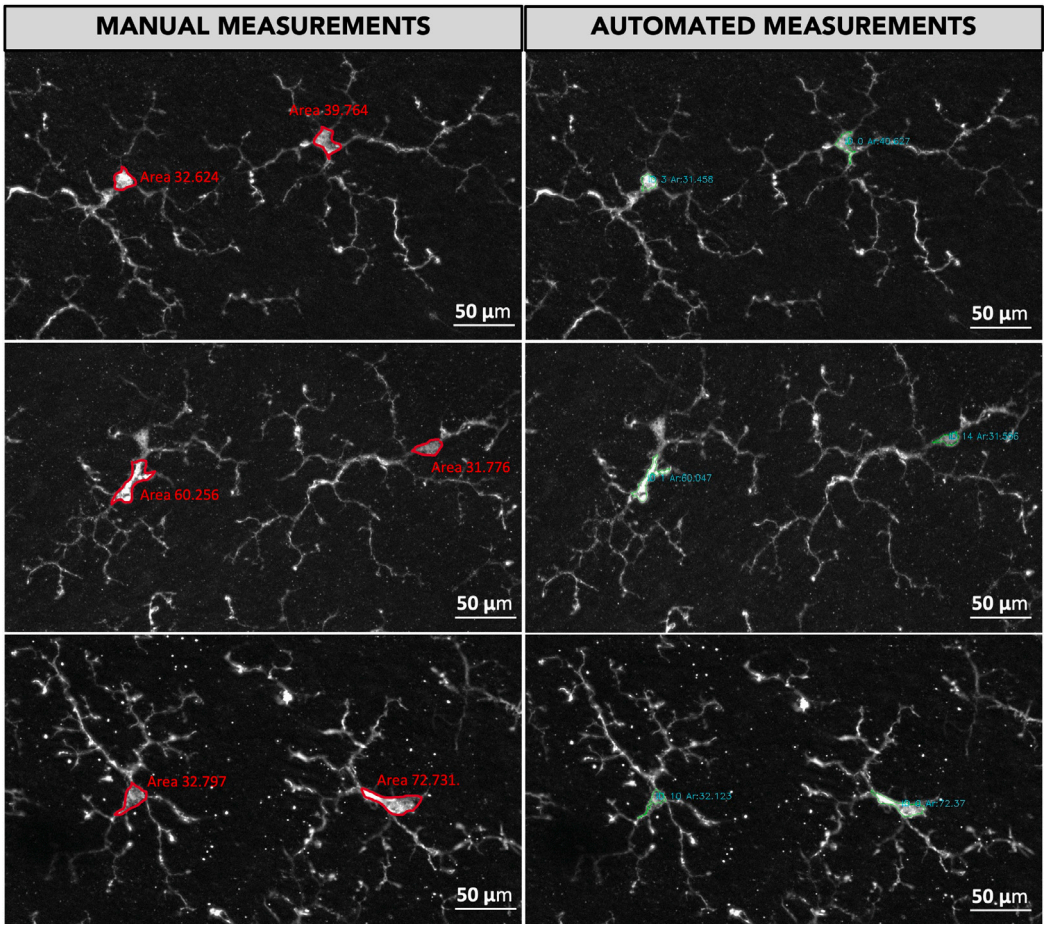

Fig. 10. Comparison of manual and automated microglial soma measurements. The left column shows manual measurements, where soma areas are outlined in red and labeled with their corresponding values. The right column displays the automated measurements obtained using the proposed software, with detected soma areas highlighted in green.

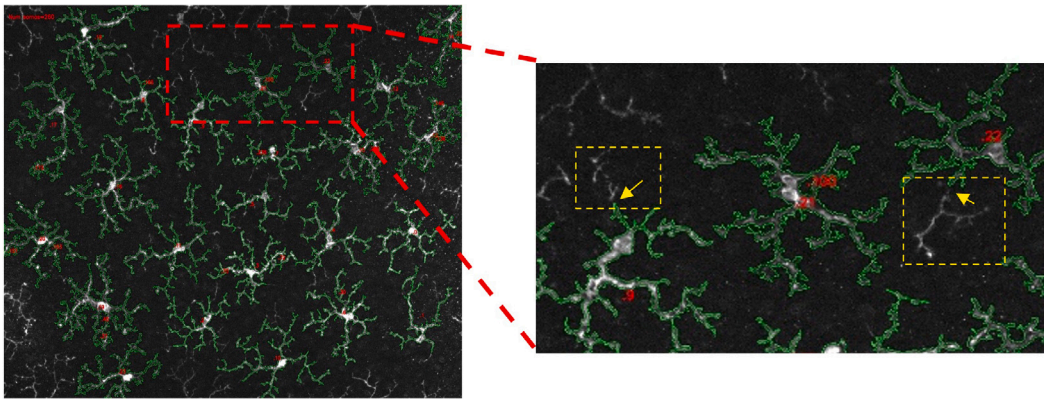

Fig. 11. Illustration of skeletonization results. The left panel shows a global view of the processed image, while the right panel presents a zoomed-in region highlighting discrepancies in skeleton continuity (yellow dashed boxes, yellow arrows). These gaps may arise due to image acquisition artifacts or cellular migration between the inner and outer plexiform layers.

conditions, where microglia tend to cluster and exhibit more complex structural alterations. These results support the software's potential for unbiased and reproducible microglial analysis in neurodegenerative disease research.

4. Discussion

In the current study, we introduce a new tool for the automatic detection retinal microglia. This automated image analysis tool developed for the counting and analysis of retinal microglial cells provides a diverse set of powerful capabilities, encompassing somas detection, quantification, and characterization, as well as skeletonization and precise calculation of arborization areas.

Improvements over the last decade in high-performance cluster computing, machine learning algorithms and image classification frameworks based on deep learning architectures indicate that the field of imaging in biomedical sciences is entering a new era of automated analysis [49,50].

Different manual and automated methods have been used for analyzing retinal microglial morphology parameters. Manual methods,

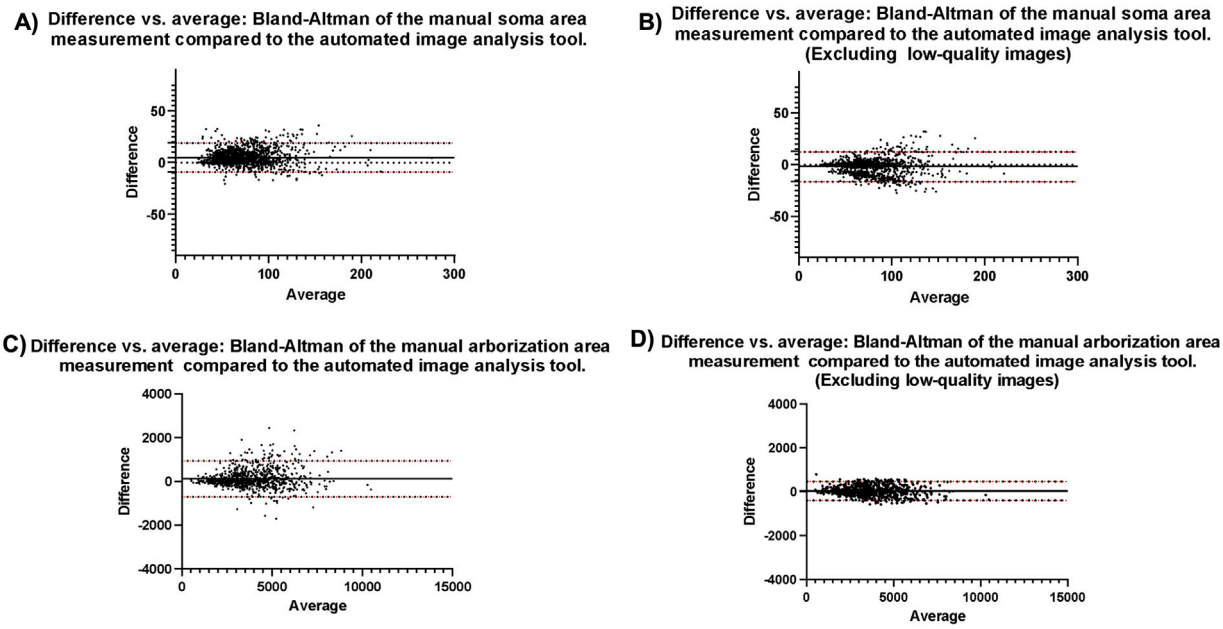

Fig. 12. The Bland-Altman plots show the differences in area between the manual measurements and those provided by the automatic tool: (A) Soma area with all images (B) Soma area after removing low quality images and (C) Arborization areas with all images and (D) Arborization areas after removing low quality images. *The X-axis represents the average of the automatic and manual measurements, while the Y-axis displays the differences between them. The black line shows the average of the differences. The red dotted lines show the limits of agreement.*

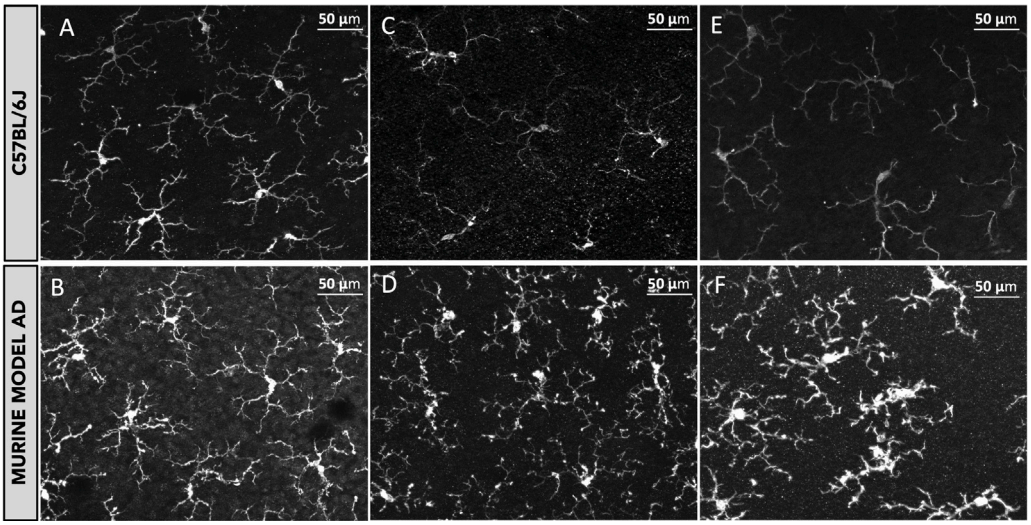

Fig. 13. Comparison of retinal microglia between a healthy control (C57BL/6J) and a murine model of Alzheimer's disease (AD) (A, C, E) Microglial morphology in the control group (C57BL/6J). (B, D, F) Microglial morphology in the Alzheimer's disease model.

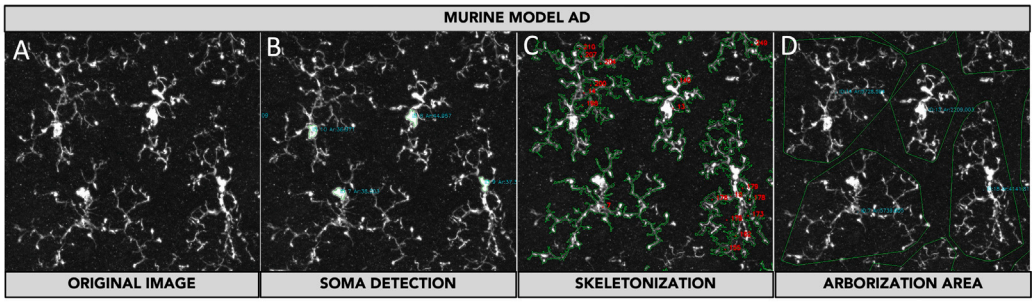

Fig. 14. Automated analysis of retinal microglia in a murine model of AD using the proposed software. (A) Original microscopy image of microglial cells. (B) Automated soma detection (highlighted in blue). (C) Skeletonization process, illustrating the microglial structure in green. (D) Arborization area measurement, outlining the detected regions in green.

such as those presented in [18,51], used for quantification and classification of retinal microglia have several drawbacks: (i) the substantial time required to analyze images, (ii) inter-rater biases, (iii) the complexity of making completely blind measurements in studies comparing microglia between disease models with different microglial characteristics, and (iv) the tendency of researchers to select the "easiest" cells to characterize, i.e., the ones that are isolated and have little overlap with the processes of other cells [47]. This bias, although understandable, may affect the morphometric measurements taken, especially in the microglial analysis of diseases such as Alzheimer's disease where microglia may localize and overlap around Beta amyloid plaques or phagocytose Tau protein and it is complex to delineate which processes may overlap [52].

To overcome the limitations of manual microglial analysis, our software offers a fully automated framework for soma detection, skeletonization, and arborization measurements, reducing human bias and improving reproducibility. Although the primary validation was performed using a healthy animal model, we also tested the tool in a murine model of Alzheimer's disease (see Section 3.2), with encouraging results. Even in this more complex and variable context, the software was able to accurately identify and quantify microglial features, capturing the structural changes typically associated with neurodegeneration. These results suggest that the tool is not only reliable under controlled conditions but also adaptable to the challenges posed by pathological tissue. We believe this flexibility makes it a valuable resource for researchers studying microglial behavior in disease. Looking ahead, applying the software to larger and more diverse datasets will be key to expanding its utility and exploring its potential role in translational and clinical research.

Our tool not only facilitates comprehensive analysis of microglial cell numbers and characteristics but also ensures precise and rapid processing. The algorithmic nature of our tool guarantees consistent and deterministic results over time and across different samples. Besides, our program offers a remarkable reduction in analysis time, enabling automatic image analysis that surpasses human capabilities by over 1000 times: the analysis of the set of 1702 images has taken around 1 year for one expert vs. 8 h of computation. By eliminating human fatigue and streamlining the research workflow, our tool enhances efficiency and productivity to an unprecedented level. This enables researchers to process larger volumes of data, increasing the statistical power and enhancing the reliability of their findings. In addition to this performance, preliminary input from early users of the software indicated that the tool was intuitive to use and substantially reduced the time required for analysis while improving consistency across datasets. Users especially valued the ability to process large batches of images and visualize results in real time. Suggestions for future versions included the implementation of a quality flagging system and greater flexibility in output customization, further supporting the tool's usability and relevance in experimental workflows.

The variation between computed and manual area (see Fig. 10) can be attributed to the practices used by experts to smooth the contour of the soma and also because of the criteria for deciding the boundaries between soma and processes depends in some degree of the experts. Taking into account that 1 pixel is equivalent to 0.227 μm and that having slightly different criteria between experts could represent 40 pixels in a typical area of 50 μm^2, which implies a typical difference of 4.1% between the computed value and the area of the soma manually measure and even different values for the area of the soma measured by different experts. This discrepancy between expert serves the point that manual classification struggles with inter-rater reproducibility, especially between different research groups [29,47].

Although automated methods for analyzing microglia are gaining popularity, few are suitable for retinal use [36,38]. Among these, [36] introduces a script to count retinal microglial cells and a method to automatically classify retinal microglial cells into five different morphotypes, based on support vector machines (SVM). The script was tested with just 30 images and the SVM performance was evaluated using only 1200 cells (240 per morphotype). Similarly, in [38], a novel segmentation routine for automated counting and morphological analysis of retinal microglia that achieves accuracy comparable to that of human experts was presented. However, only 11 images and 1600 cells were used to test their method. Likewise, an algorithm for automated counting microglial cells in mouse retinas was presented in [32], however, the performance of their method, compared to that of a human expert, was tested using only 120 images. That is, despite the great progress all these works represent, their methods were validated using a limited number of images. On the contrary, our tool was validated by comparing the results obtained by our algorithm with those obtained by an experienced observer with numerous images and cells (1702 images containing 24,559 cells) to extract quantitative data (number of microglial cells per retinal sector) as well as complex morphology data (areas of arborization and skeletonization). This gives our work greater statistical precision, better representation of cell variability, greater robustness to variable conditions and ultimately greater reliability to our research. Despite machine learning algorithms like SVM and convolutional neural network (CNN) offer similar results for true positive rates and true negative rates [37] our tool is based on rules validated with experts which provides systematic results to the same inputs with less computation resources and getting rid of previous training. In addition, our tool can be used with no initial validated and/or training data set at the same time that takes the benefits of soma validated when used by experts.

Another problem that researchers may encounter is the variation in image quality. This variation can be attributed to several factors, including the perfusion and fixation of animal tissues, the cleanliness of the mounting medium, the immunoreactivity of the antibodies used, and the specific layer of the retina being photographed (capturing images from the outer plexiform layer (OPL) differs from the inner plexiform layer (IPL), with the former often displaying less noise than the latter). Consequently, during image acquisition, our priority is to photograph sectors with fewer artifacts to minimize the presence of noise and ensure the best possible image quality. Our software demonstrates the ability to analyze low-quality images that a human analyst might discard if tasked with manual analysis. While medical experts endeavor not to discard images due to the ethical implications involved, as they require the sacrifice of laboratory animals, there are instances where they must make the difficult decision to discard them if they contain significant noise and very low quality. It is crucial to highlight that our algorithm detects more somas than experts would identify through visual inspection. As a result, the implementation of the algorithm allows effectively reducing the number of discarded images. More importantly, despite 20.92% of the images obtained from the microscope were of low quality, and after being analyzed by our tool having that the experimental results achieved match or exceed that of other studies: the soma detection yielded an F1-score of 0.94, being the recall and precision 0.97 and 0.92 respectively. Removing low-quality images significantly enhanced performance, raising the F1-score and precision to 0.97, while reducing the false positive rate to 2.84%. Meanwhile, recall remained consistent at 0.97, confirming the method's robustness under optimal conditions. Nevertheless, retaining the ability to process low-quality images is valuable, as it enhances dataset usability and reduces the need for animal sacrifices. While expert input can be used to refine thresholding, our tool offers a significant advantage over manual analysis by fully automating soma detection, skeletonization, and arborization measurements - features not available in conventional image analysis pipelines.

To the best of our knowledge, no tool apart from ours can automatically analyze skeletonization and calculate the arborization area of cells. This capacity is a significant breakthrough in the field of neuroinflammation research because it allows for the analysis of the transition from quiescent microglia to morphological types displaying activation, providing invaluable insights into the early stages of

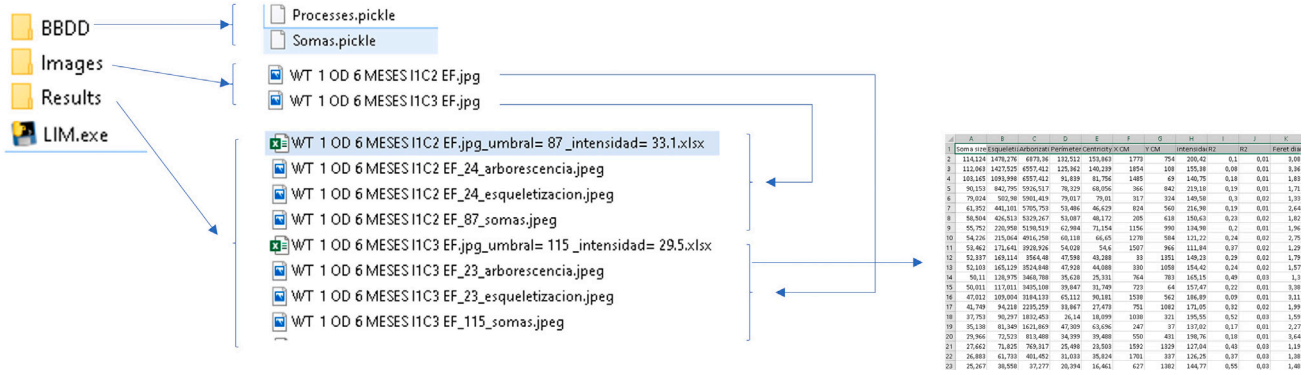

Fig. A.1. File structure of the system, illustrating the organization of databases (BBDD), input images, results, and executable files. The 'Results' folder contains processed images and spreadsheets with computed morphological data.

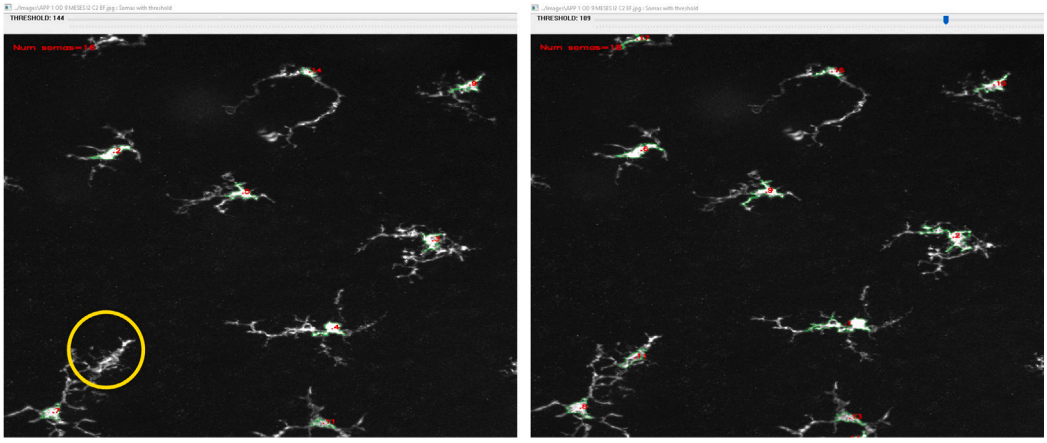

Fig. A.2. Graphical User Interface for threshold selecting (Step 8). (Left: threshold computed automatically; right: threshold fine-tuned by the expert in case of need).

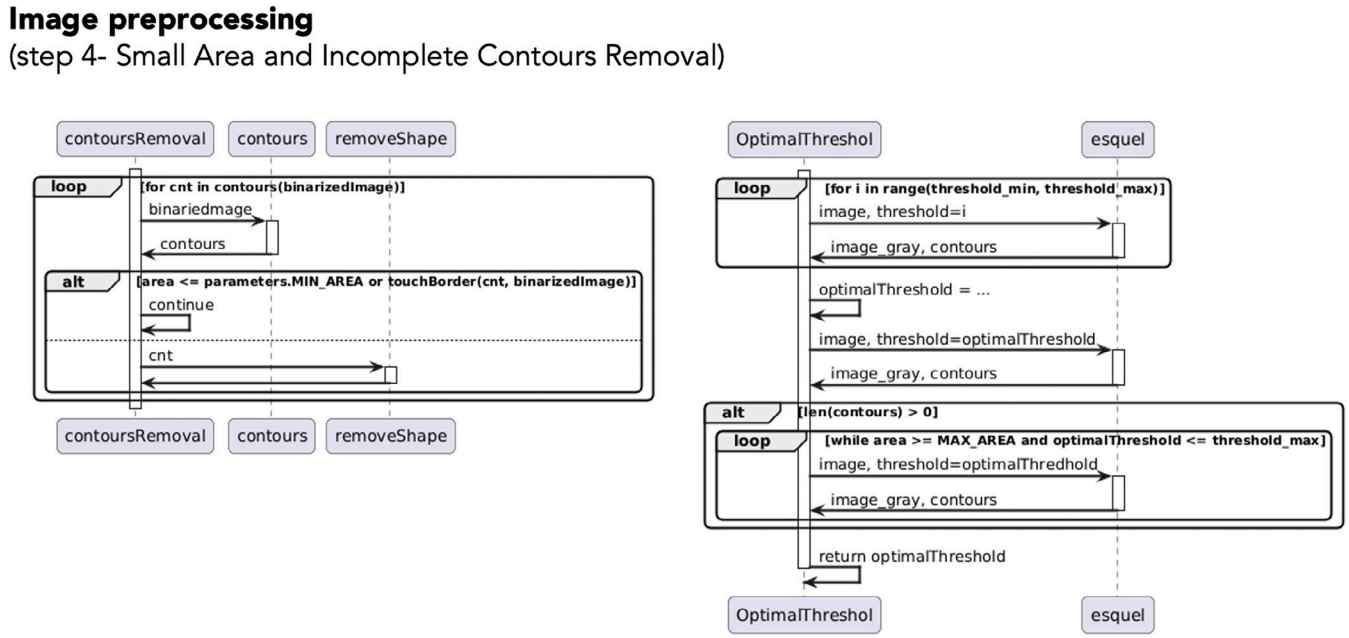

Fig. B.1. Sequence diagrams illustrating the image preprocessing Step 4.

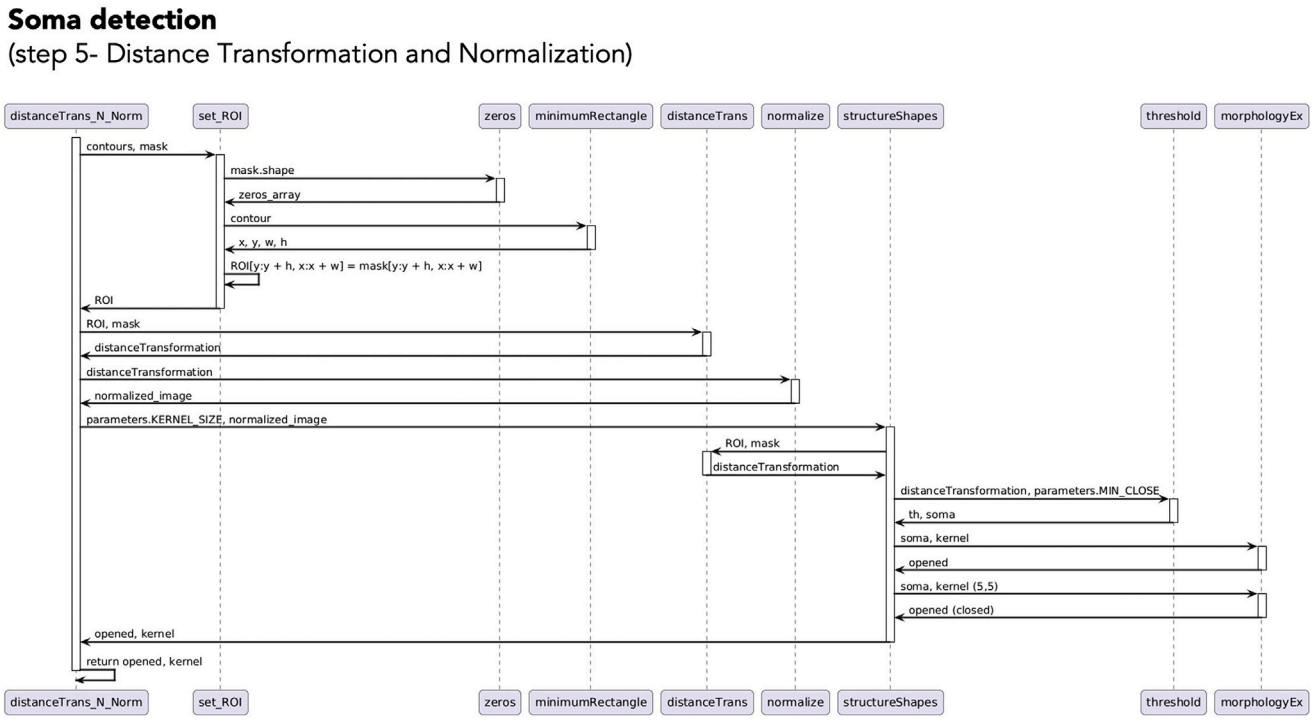

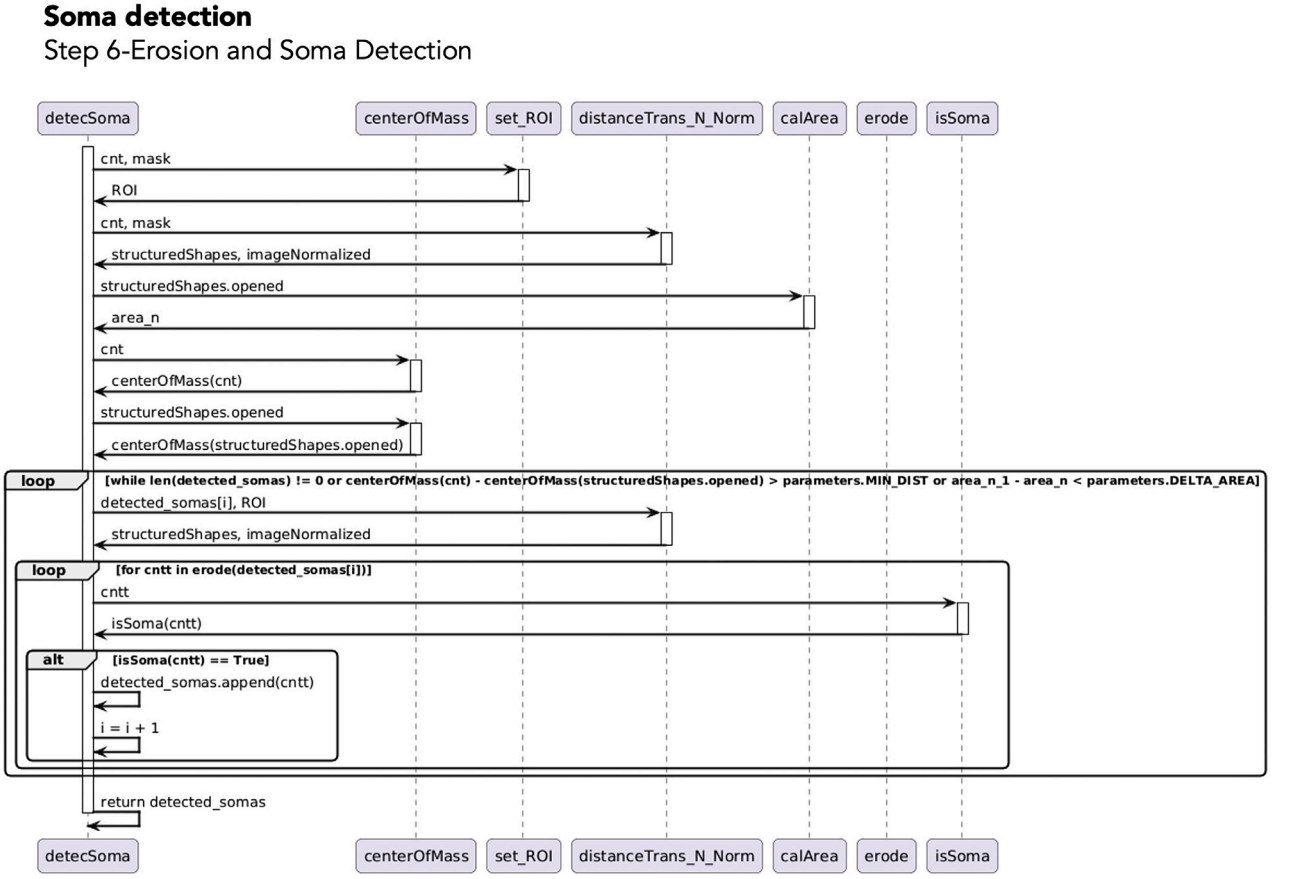

Fig. B.2. Sequence diagrams illustrating the image preprocessing Steps 5–6.

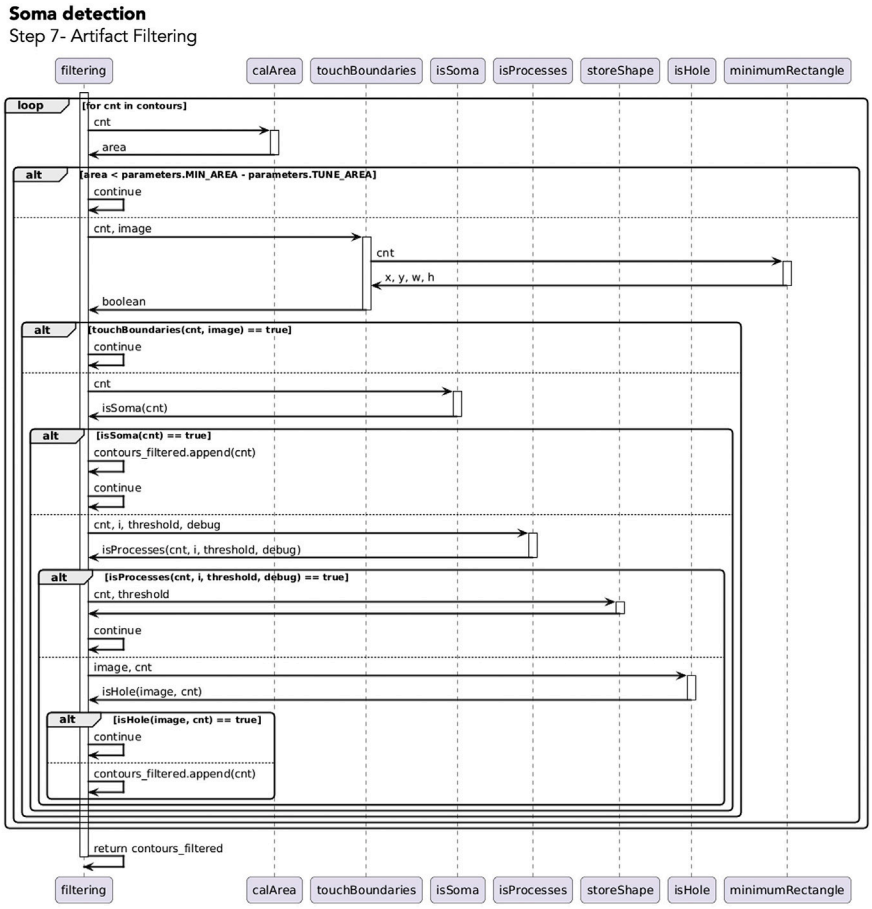

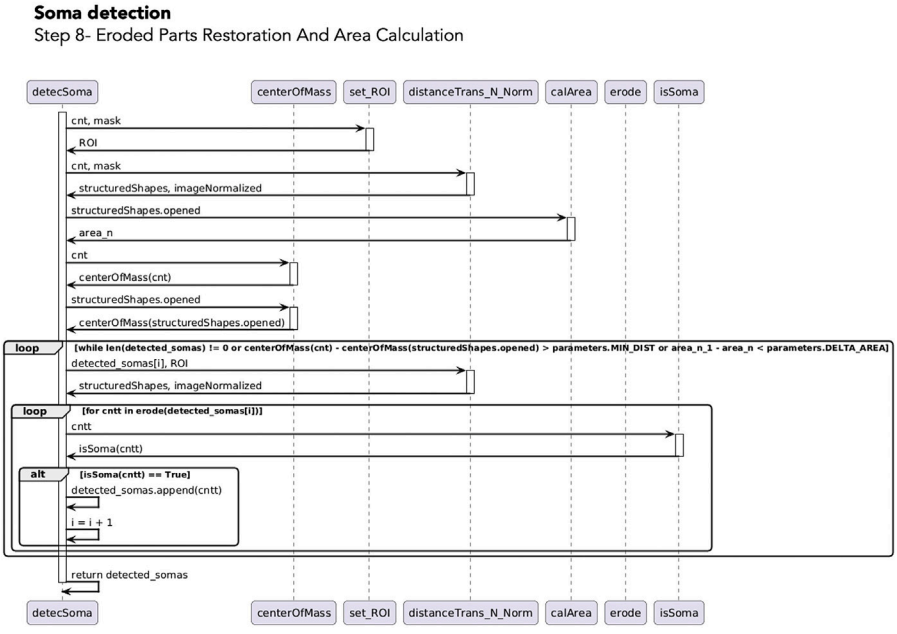

Fig. B.3. Sequence diagrams illustrating the image preprocessing Steps 7–8.

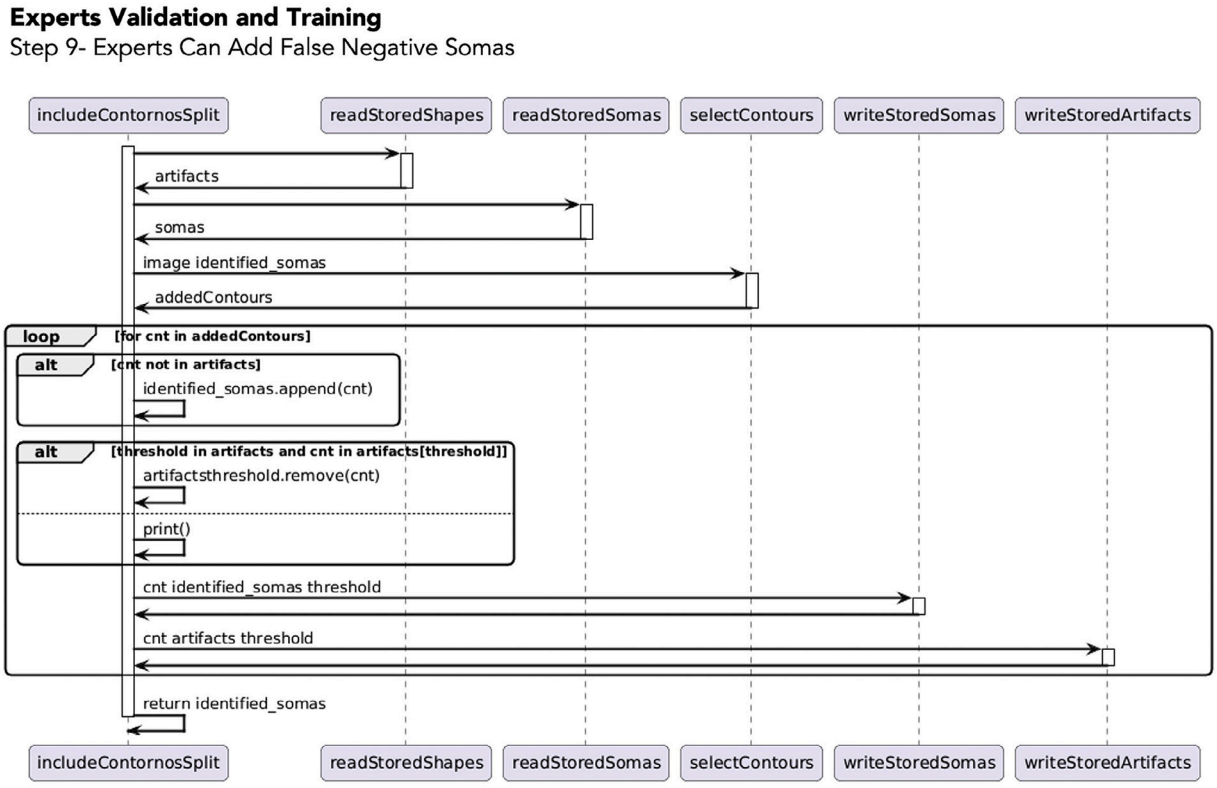

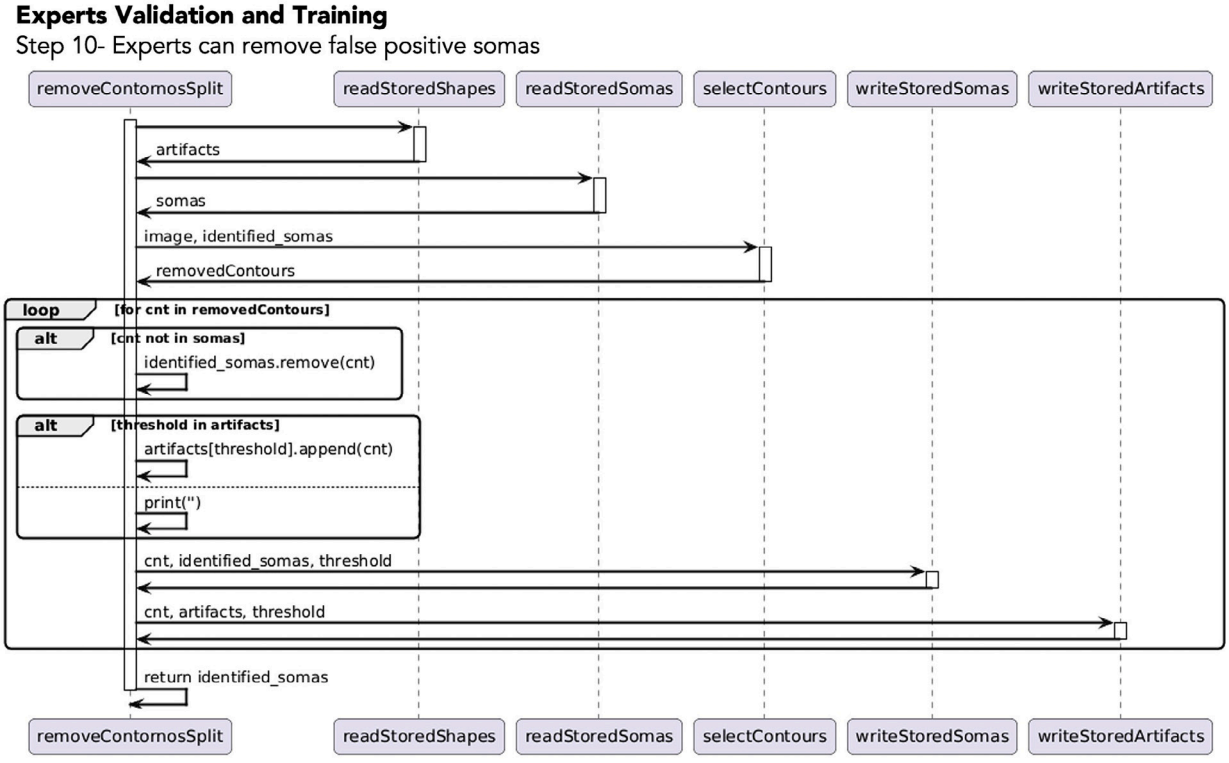

Fig. B.4. Sequence diagrams illustrating the image preprocessing Steps 9–10.

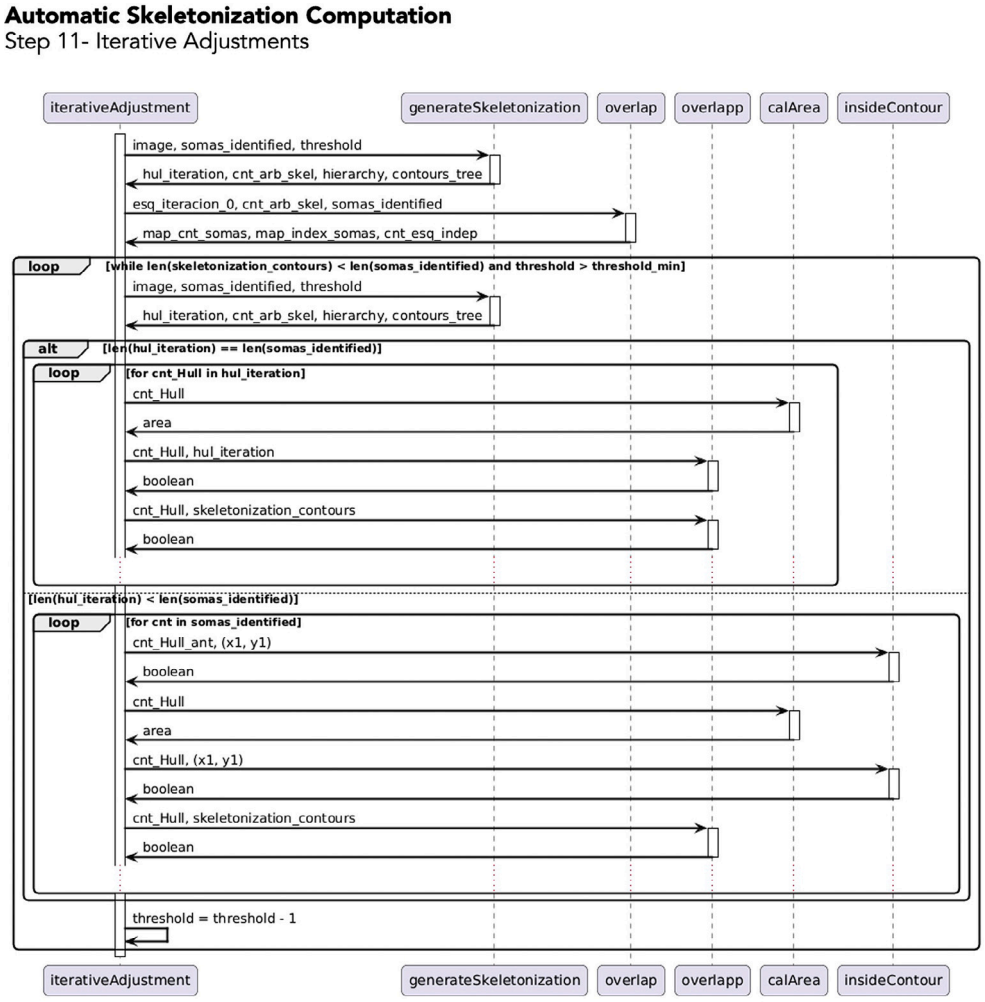

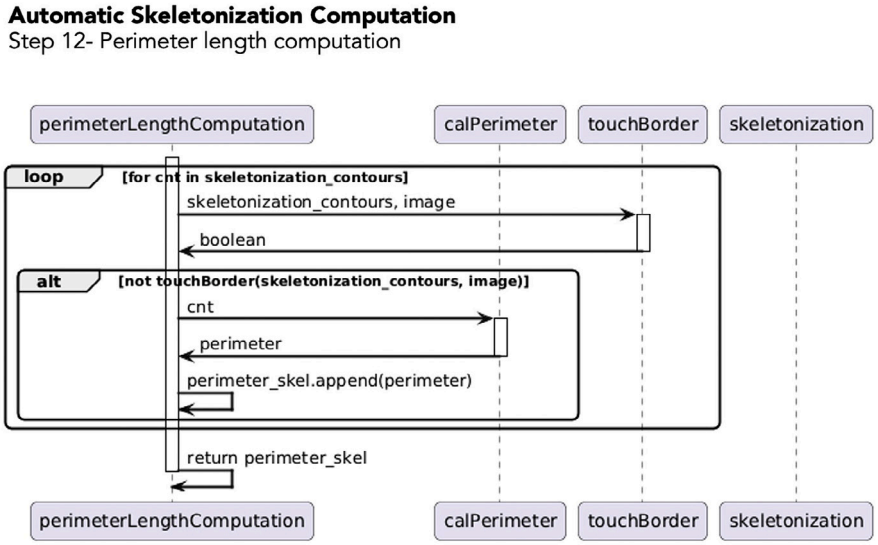

Fig. B.5. Sequence diagrams illustrating the image preprocessing Steps 11–12.

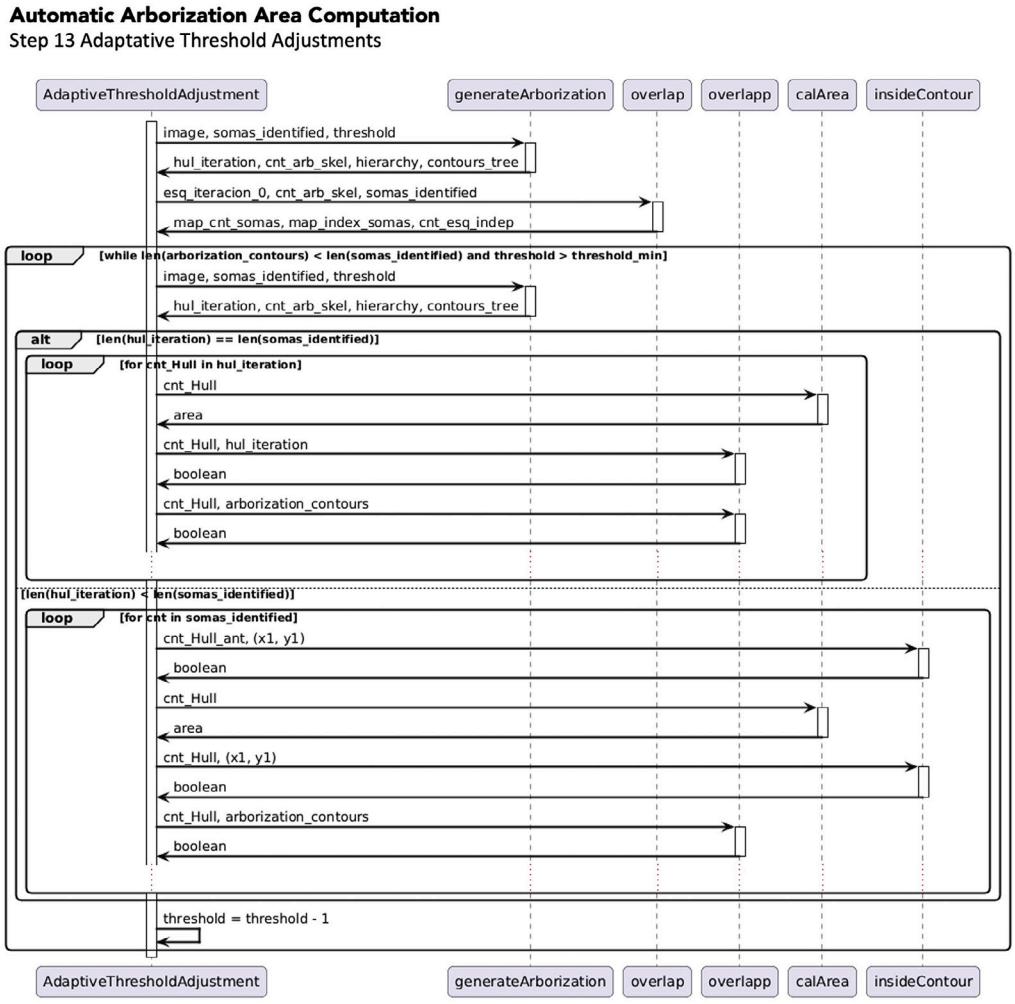

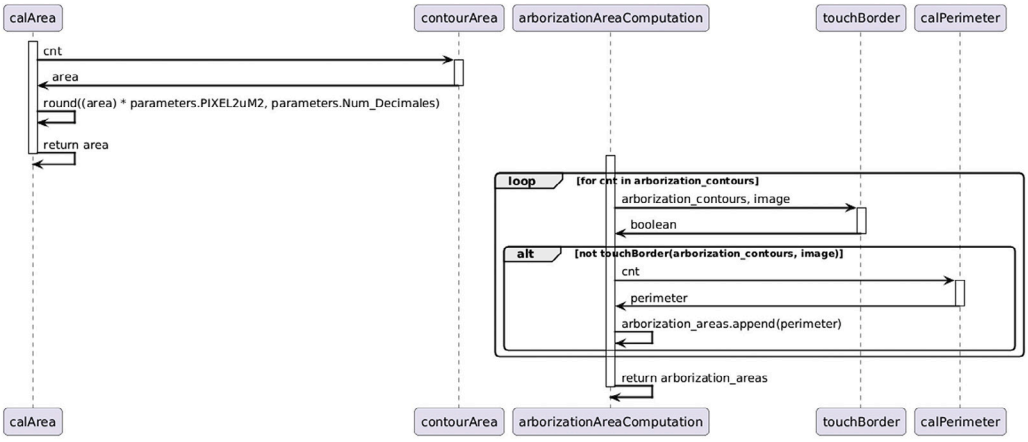

Fig. B.6. Sequence diagrams illustrating the image preprocessing Steps 13–14.

neuroinflammation and into the pivotal role of microglia in disease progression. Our software accomplishes this skeletonization analysis and calculation arborization area of cells with remarkable accuracy since a mean absolute percentage error (MAPE) of 9.12% and 8.67% were obtained when calculating the areas of somas and the arborization areas, respectively. Furthermore, excluding lower-quality images enhanced measurement accuracy, improving the MAPE to 8.85% for soma areas and 8.25% for arborization areas, demonstrating the benefits of high-quality image selection in ensuring precise quantification.

The results of this study demonstrate a high concordance between manual and automatic measurements for both soma area and arborization area. The intraclass correlation coefficients (ICC) were consistently high, indicating excellent reliability. Additionally, the Bland-Altman analyses showed narrow limits of agreement and low biases, both for the full set of images and after excluding low-quality images. These findings support the validity of automatic measurements as a precise and reliable alternative to manual measurements, facilitating analysis in future studies.

The vast majority of the automated approaches revolve around segmentation process based on a single threshold defined and set manually by the user which is used to generate a binary image separating somas and processes from background. This is followed by denoising and filtering noise to remove staining contours. The resulting binary image is masked according to the identified ROI hiding the original background image which allow medical experts to compare with the original image provided by the microscope [38]. In our case, a range of threshold values are used to completely cover the somas, and the resulting contours are correlated for soma identification, and always keeping the original image as background so as to provide medical experts with the full context. Thus, another essential advantage of our tool lies in its capacity to empower experts to manipulate the acquired results effectively having always as background image the raw images provided by the microscope so they can compare the raw and the processed images without any mask. This essential feature has not been identified in other tools. Through this interactive feature, experts can add or remove detected somas, fine-tune the skeletonization of cells by adding or removing elements, and make adjustments to the polygon representing the cell's arborization area. This level of control ensures that the final outcome benefits from the expert's insightful supervision, if deemed necessary. Moreover, by offering this interactivity, we establish an automated, yet thorough evaluation of the initial results obtained by the tool before any modifications are introduced by the expert, ensuring precision and confidence in the analysis process.

Another key consideration when designing our tool was the feasibility of 3D image acquisition. The tool could be improved to provide 3D images. However, with the Zeiss Axioplan 2 fluorescence microscope, obtaining 3D images would require performing a Z-Stack of each cell, which implies a processing time of approximately 30 min per cell for each image. In this study, a total of 24,559 cells have been analyzed, which would mean 736,770 min solely for 3D acquisition. This process would be extremely time-consuming and does not align with our goal of analyzing all microglial cells in a short time. Our current 2D approach allows for fast and efficient analysis of many cells, which is crucial in the early stages of research for large-scale studies.

In summary, our tool offers several compelling advantages that enhance the analysis of complex and diverse images. Firstly, the implementation of multiple binarization thresholds within an image proves especially valuable when dealing with heterogeneous samples. This dynamic approach enables our tool to adaptively adjust the threshold for different regions, leading to significantly more precise and accurate results. Secondly, our algorithm's exceptional capability to analyze low-quality images sets it apart from human experts who might dismiss such images due to their limitations. This proficiency allows for the examination of diverse samples that would otherwise be considered suboptimal in image quality. As addressed above ethical considerations come into play, as our tool's ability to analyze low-quality images reduces the need for a larger number of mice sacrifices [43], thus minimizing the use of animals in research and maximizing the utilization of available resources, enhancing the comprehensiveness of the analysis.

Furthermore, the interaction between our tool and the expert produces results that hold immense value beyond immediate analysis. The data gathered from this collaboration serves a dual purpose, not only providing crucial insights but also laying the groundwork for training an expert system in the future. By harnessing this wealth of information, our tool gains the potential for automatic improvement through the integration of cutting-edge artificial intelligence algorithms. This seamless combination of expertise and technology ensures a continuous evolution of the tool's capabilities, making it an invaluable asset for ongoing research and analysis.

5. Conclusions

This paper presents a novel software specifically designed for the automated counting and detail analysis of retinal microglia, overcoming key limitations of manual methods while maintaining high accuracy and reproducibility. By integrating automated soma detection, skeletonization, and arborization measurements, the proposed tool significantly enhances microglial analysis. To the best of our knowledge, this the first software capable of automating both microglial skeletonization and arborization measurements, offering a more comprehensive assessment of microglial morphology.

One of the software's main advantages is its ability to analyze both high- and low-quality images, which are often encountered during image acquisition. This feature is not only technically beneficial but also ethically significant, as it maximizes the use of collected samples and reduces the need for additional animal sacrifices. Additionally, its efficiency and scalability enable the processing of large datasets, facilitating more extensive and detailed studies in microglia research.

Ultimately, this study represents an important step toward standardized and automated microglial analysis, offering a powerful tool for investigating microglial dynamics and their involvement in neurological and pro-inflammatory disorders. Future work will focus on expanding its applications to neurodegenerative disease research.

CRediT authorship contribution statement

Miguel A. Sánchez-Puebla: Writing – review & editing, Writing – original draft, Visualization, Validation, Supervision, Software, Resources, Project administration, Methodology, Investigation, Funding acquisition, Formal analysis, Data curation, Conceptualization. **Lidia Sánchez-Puebla:** Writing – review & editing, Writing – original draft, Visualization, Validation, Supervision, Resources, Methodology, Investigation, Formal analysis, Data curation, Conceptualization. **Ana Granados:** Writing – review & editing, Writing – original draft, Visualization, Validation, Supervision, Methodology, Investigation, Formal analysis. **Valentín Moreno:** Writing – review & editing, Visualization, Validation, Supervision, Methodology, Investigation, Formal analysis. **Inés López-Cuenca:** Writing – review & editing, Writing – original draft, Visualization, Validation, Supervision, Resources, Investigation, Formal analysis. **Ana I. Ramírez:** Writing – review & editing, Validation, Supervision, Resources, Methodology, Investigation, Data curation. **José M. Ramírez:** Writing – review & editing, Validation, Supervision, Resources, Investigation. **Juan Llorens:** Writing – review & editing, Validation, Supervision, Investigation.

Code and dataset availability

The software described in this article is currently undergoing intellectual property registration with the reference number 09/688017.9/25. The source code (over 10,000 lines of code executed with Python interpreter 3.8) implemented for this tool and the dataset are available and can be provided upon request.

Funding

Lidia Sánchez-Puebla is currently supported by a Predoctoral Fellowship (CT82/20-CT83/20) from the Complutense University of Madrid.

Declaration of competing interest

The authors declare that they have no known competing financial interests or personal relationships that could have appeared to influence the work reported in this paper.

Appendix A. Software execution and user interaction workflow

The tool is launched by selecting its application icon. Upon execution, it automatically processes all images stored in the 'Images' folder, supporting common formats such as JPEG, JPG, PNG, and BITMAP. Images are analyzed sequentially, and for each input, the tool generates three output images—soma detection, skeletonization, and arborization—along with an Excel file containing the corresponding morphological analysis data. All results are saved in the 'Results' folder (see Fig. A.1).

After processing each image, the tool automatically transfers the confirmed soma and cell processes to the 'BBDD' folder for further use in steps 6-7.

At step 8, the tool pauses, allowing the user to adjust the threshold using a track bar (Fig. A.2) if necessary. If the threshold is modified, the tool reprocesses the image starting from step 5, updating the soma identification accordingly. This adjustment can be repeated as many times as needed.

Pressing the 'Escape' key advances the tool to step 9 and subsequently to step 10 (Fig. 5), where users can manually refine the arborization perimeter by dragging and repositioning points as needed.

Appendix B. Sequence diagrams

This section presents the sequence diagrams used in the study, providing a visual representation of the interaction flow between system components (see Figs. B.1–B.6).

References

[1] D. Nayak, T.L. Roth, D.B. McGavern, Microglia development and function, Annu. Rev. Immunol. 32 (1) (2014) 367–402, http://dx.doi.org/10.1146/annurev-immunol-032713-120240.

[2] A. Gallego, Chapter 7 comparative studies on horizontal cells and a note on microglial cells, Prog. Retin. Res. 5 (1986) 165–206, http://dx.doi.org/10.1016/0278-4327(86)90010-6.

[3] P. del Río Hortega, El tercer elemento de los centros nerviosos. I. La microglía en estado normal, Boletín de la Soc. Española de Biología 9 (1919) 68–82.

[4] M.B. Graeber, W.J. Streit, Microglia: biology and pathology, Acta Neuropathol. 119 (1) (2010) 89–105, http://dx.doi.org/10.1007/s00401-009-0622-0.

[5] S. Jinno, F. Fleischer, S. Eckel, V. Schmidt, T. Kosaka, Spatial arrangement of microglia in the mouse hippocampus: A stereological study in comparison with astrocytes, Glia 55 (13) (2007) 1334–1347, http://dx.doi.org/10.1002/glia.20552, _eprint: https://onlinelibrary.wiley.com/doi/pdf/10.1002/glia.20552.

[6] W. Eric Thomas, Brain macrophages: evaluation of microglia and their functions, Brain Res. Rev. 17 (1) (1992) 61–74, http://dx.doi.org/10.1016/0165-0173(92)90007-9.

[7] A.M. Santos, R. Calvente, M. Tassi, M.-C. Carrasco, D. Martín-Oliva, J.L. Marín-Teva, J. Navascués, M.A. Cuadros, Embryonic and postnatal development of microglial cells in the mouse retina, J. Comp. Neurol. 506 (2) (2008) 224–239, http://dx.doi.org/10.1002/cne.21538, _eprint: https://onlinelibrary.wiley.com/doi/pdf/10.1002/cne.21538.

[8] P. Sobrado-Calvo, M. Vidal-Sanz, M.P. Villegas-Pérez, Rat retinal microglial cells under normal conditions, after optic nerve section, and after optic nerve section and intravitreal injection of trophic factors or macrophage inhibitory factor, J. Comp. Neurol. 501 (6) (2007) 866–878, http://dx.doi.org/10.1002/cne.21279, _eprint: https://onlinelibrary.wiley.com/doi/pdf/10.1002/cne.21279.

[9] N. Cuenca, L. Fernández-Sánchez, L. Campello, V. Maneu, P. De la Villa, P. Lax, I. Pinilla, Cellular responses following retinal injuries and therapeutic approaches for neurodegenerative diseases, Prog. Retin. Eye Res. 43 (2014) 17–75, http://dx.doi.org/10.1016/j.preteyeres.2014.07.001.

[10] M.-E. Tremblay, B. Stevens, A. Sierra, H. Wake, A. Bessis, A. Nimmerjahn, The role of microglia in the healthy brain, J. Neurosci. 31 (45) (2011) 16064–16069, http://dx.doi.org/10.1523/JNEUROSCI.4158-11.2011, Publisher: Society for Neuroscience Section: Symposium and Mini-Symposium.

[11] F.R. Walker, S.B. Beynon, K.A. Jones, Z. Zhao, R. Kongsui, M. Cairns, M. Nilsson, Dynamic structural remodelling of microglia in health and disease: A review of the models, the signals and the mechanisms, Brain Behav. Immun. 37 (2014) 1–14, http://dx.doi.org/10.1016/j.bbi.2013.12.010.

[12] S.A. Wolf, H. Boddeke, H. Kettenmann, Microglia in physiology and disease, Annu. Rev. Physiol. 79 (2017) 619–643, http://dx.doi.org/10.1146/annurev-physiol-022516-034406.

[13] A. Ramírez, B. Rojas, R. de Hoz, J.J. Salazar, B. Gallego, A. Triviño, J. Ramírez, Microglia, inflammation, and glaucoma, Glaucoma (2015) 1–16.

[14] B. Gallego, Implicación de la glía retiniana en un modelo experimental del glaucoma (Ph.D. thesis), Universidad Complutense de Madrid, 2015.

[15] A.I. Ramírez, R. de Hoz, E. Salobrar-Garcia, J.J. Salazar, B. Rojas, D. Ajoy, I. López-Cuenca, P. Rojas, A. Triviño, J.M. Ramírez, The role of microglia in retinal neurodegeneration: Alzheimer's disease, parkinson, and glaucoma, Front. Aging Neurosci. 9 (2017) http://dx.doi.org/10.3389/fnagi.2017.00214.

[16] M. Karlstetter, S. Ebert, T. Langmann, Microglia in the healthy and degenerating retina: Insights from novel mouse models, Immunobiology 215 (9) (2010) 685–691, http://dx.doi.org/10.1016/j.imbio.2010.05.010.

[17] W.J. Streit, N.W. Sammons, A.J. Kuhns, D.L. Sparks, Dystrophic microglia in the aging human brain, Glia 45 (2) (2004) 208–212, http://dx.doi.org/10.1002/glia.10319, _eprint: https://onlinelibrary.wiley.com/doi/pdf/10.1002/glia.10319.

[18] A.I. Ramírez, R. de Hoz, J.A. Fernández-Albarral, E. Salobrar-Garcia, B. Rojas, F.J. Valiente-Soriano, M. Avilés-Trigueros, M.P. Villegas-Pérez, M. Vidal-Sanz, A. Triviño, J.M. Ramírez, J.J. Salazar, Time course of bilateral microglial activation in a mouse model of laser-induced glaucoma, Sci. Rep. 10 (1) (2020) 4890, http://dx.doi.org/10.1038/s41598-020-61848-9.

[19] Z. Ji, C. Liu, W. Zhao, C. Soto, X. Zhou, Multi-scale modeling for systematically understanding the key roles of microglia in AD development, Comput. Biol. Med. 133 (2021) 104374, http://dx.doi.org/10.1016/j.compbiomed.2021.104374.

[20] A. Gómez-Pascual, T. Naccache, J. Xu, K. Hooshmand, A. Wretlind, M. Gabrielli, M.T. Lombardo, L. Shi, N.J. Buckley, B.M. Tijms, S.J.B. Vos, M. ten Kate, S. Engelborghs, K. Sleegers, G.B. Frisoni, A. Wallin, A. Lleó, J. Popp, P. Martinez-Lage, J. Streffer, F. Barkhof, H. Zetterberg, P.J. Visser, S. Lovestone, L. Bertram, A.J. Nevado-Holgado, A. Gualerzi, S. Picciolini, P. Proitsi, C. Verderio, J.A. Botía, C. Legido-Quigley, Paired plasma lipidomics and proteomics analysis in the conversion from mild cognitive impairment to Alzheimer's disease, Comput. Biol. Med. 176 (2024) 108588, http://dx.doi.org/10.1016/j.compbiomed.2024.108588.

[21] G. Solana-Lavalle, R. Rosas-Romero, Classification of PPMI MRI scans with voxel-based morphometry and machine learning to assist in the diagnosis of Parkinson's disease, Comput. Methods Programs Biomed. 198 (2021) 105793, http://dx.doi.org/10.1016/j.cmpb.2020.105793.

[22] S. Siuly, S.K. Khare, E. Kabir, M.T. Sadiq, H. Wang, An efficient Parkinson's disease detection framework: Leveraging time-frequency representation and AlexNet convolutional neural network, Comput. Biol. Med. 174 (2024) 108462, http://dx.doi.org/10.1016/j.compbiomed.2024.108462.

[23] P. Rojas, A.I. Ramírez, M. Cadena, J.A. Fernández-Albarral, E. Salobrar-García, I. López-Cuenca, I. Santos-García, E. de Lago, J.L. Urcelay-Segura, J.M. Ramírez, R. de Hoz, J.J. Salazar, Retinal ganglion cell loss and microglial activation in a SOD1G93A mouse model of amyotrophic lateral sclerosis, Int. J. Mol. Sci. 22 (4) (2021) 1663, http://dx.doi.org/10.3390/ijms22041663.

[24] M. Neumann, H. Kothare, V. Ramanarayanan, Multimodal speech biomarkers for remote monitoring of ALS disease progression, Comput. Biol. Med. 180 (2024) 108949, http://dx.doi.org/10.1016/j.compbiomed.2024.108949.

[25] M. Keita, K. McIntyre, L.N. Rodden, K. Schadt, D.R. Lynch, Friedreich ataxia: clinical features and new developments, Neurodegener. Dis. Manag. 12 (5) (2022) 267–283, http://dx.doi.org/10.2217/nmt-2022-0011.

[26] A.I. Ramírez, J.A. Fernández-Albarral, R.d. Hoz, I. López-Cuenca, E. Salobrar-García, P. Rojas, F.J. Valiente-Soriano, M. Avilés-Trigueros, M.P. Villegas-Pérez, M. Vidal-Sanz, A. Triviño, J.J. Salazar, J.M. Ramírez, Chapter 6 - Microglial changes in the early aging stage in a healthy retina and an experimental glaucoma model, Progress in Brain Research 256 (1) (2020) 125–149, http://dx.doi.org/10.1016/bs.pbr.2020.05.024.

[27] Y. Hagiwara, J.E.W. Koh, J.H. Tan, S.V. Bhandary, A. Laude, E.J. Ciaccio, L. Tong, U.R. Acharya, Computer-aided diagnosis of glaucoma using fundus images: A review, Comput. Methods Programs Biomed. 165 (2018) 1–12, http://dx.doi.org/10.1016/j.cmpb.2018.07.012.

[28] X. Xue, D. Zhang, C. Sun, Y. Shi, R. Wang, T. Tan, P. Gao, S. Fan, G. Zhai, M. Hu, Y. Wu, Xiaoqing: A q&a model for glaucoma based on LLMs, Comput. Biol. Med. 174 (2024) 108399, http://dx.doi.org/10.1016/j.compbiomed.2024.108399.

[29] N. Chaaya, A. Jacques, A. Belmer, K. Beecher, S.A. Ali, F. Chehrehasa, A.R. Battle, L.R. Johnson, S.E. Bartlett, Contextual fear conditioning alter microglia number and morphology in the rat dorsal hippocampus, Front. Cell. Neurosci. 13 (2019) http://dx.doi.org/10.3389/fncel.2019.00214, Publisher: Frontiers.

[30] O.G. Holloway, A.J. Canty, A.E. King, J.M. Ziebell, Rod microglia and their role in neurological diseases, SI: Calcium signalling, Semin. Cell & Dev. Biology 94 (2019) 96–103, http://dx.doi.org/10.1016/j.semcdb.2019.02.005.

[31] H.W. Morrison, J.A. Filosa, A quantitative spatiotemporal analysis of microglia morphology during ischemic stroke and reperfusion, J. Neuroinflammation 10 (1) (2013) 782, http://dx.doi.org/10.1186/1742-2094-10-4.

[32] P.d. Gracia, B.I. Gallego, B. Rojas, A.I. Ramírez, R.d. Hoz, J.J. Salazar, A. Triviño, J.M. Ramírez, Automatic counting of microglial cells in healthy and glaucomatous mouse retinas, PLOS ONE 10 (11) (2015) e0143278, http://dx.doi.org/10.1371/journal.pone.0143278, Publisher: Public Library of Science.

[33] T.J. Kataras, T.J. Jang, J. Koury, H. Singh, D. Fok, M. Kaul, ACCT is a fast and accessible automatic cell counting tool using machine learning for 2D image segmentation, Sci. Rep. 13 (1) (2023) 8213, http://dx.doi.org/10.1038/s41598-023-34943-w.

[34] I. Suleymanova, D. Bychkov, J. Kopra, A deep convolutional neural network for efficient microglia detection, Sci. Rep. 13 (1) (2023) 11139, http://dx.doi.org/10.1038/s41598-023-37963-8.

[35] C. Kozlowski, R.M. Weimer, An automated method to quantify microglia morphology and application to monitor activation state longitudinally in vivo, PLOS ONE 7 (2) (2012) e31814, http://dx.doi.org/10.1371/journal.pone.0031814, Publisher: Public Library of Science.

[36] S. Choi, D. Hill, L. Guo, R. Nicholas, D. Papadopoulos, M.F. Cordeiro, Automated characterisation of microglia in ageing mice using image processing and supervised machine learning algorithms, Sci. Rep. 12 (1) (2022) 1806, http://dx.doi.org/10.1038/s41598-022-05815-6.

[37] J. Leyh, S. Paeschke, B. Mages, D. Michalski, M. Nowicki, I. Bechmann, K. Winter, Classification of microglial morphological phenotypes using machine learning, Front. Cell. Neurosci. 15 (2021) 701673, http://dx.doi.org/10.3389/fncel.2021.701673.

[38] N.F. Ash, M.T. Massengill, L. Harmer, A. Jafri, A.S. Lewin, Automated segmentation and analysis of retinal microglia within ImageJ, Exp. Eye Res. 203 (2021) 108416, http://dx.doi.org/10.1016/j.exer.2020.108416.

[39] S. Ramón y Cajal, Histology of the Nervous System of Man and Vertebrates, in: History of Neuroscience, Oxford University Press, 1995.

[40] R.C. Gonzalez, R.E. Woods, Digital Image Processing, fourth ed., Pearson Education, 2018.

[41] W. Burger, M.J. Burge, Digital Image Processing: An Algorithmic Introduction, in: Texts in Computer Science, Springer International Publishing, Cham, 2022, http://dx.doi.org/10.1007/978-3-031-05744-1.

[42] N. Otsu, A threshold selection method from gray-level histograms, IEEE Trans. Syst. Man Cybern. 9 (1) (1979) 62–66, http://dx.doi.org/10.1109/TSMC.1979.4310076, Conference Name: IEEE Transactions on Systems, Man, and Cybernetics.

[43] B.M. Davis, M. Salinas-Navarro, M.F. Cordeiro, L. Moons, L. De Groef, Characterizing microglia activation: a spatial statistics approach to maximize information extraction, Sci. Rep. 7 (1) (2017) 1576, http://dx.doi.org/10.1038/s41598-017-01747-8.

[44] V. Moreno, A. Ledezma, A. Sanchis, A static images based-system for traffic signs detection, in: Artificial Intelligence and Applications, 2006, pp. 445–450.

[45] J. Stoker, The wedge product and the exterior derivative of differential forms, with applications to surface theory, in: Differential Geometry, John Wiley & Sons, Ltd, 1988, pp. 335–370, http://dx.doi.org/10.1002/9781118165461.ch10.

[46] M.-K. Hu, Visual pattern recognition by moment invariants, IRE Trans. Inf. Theory 8 (2) (1962) 179–187, http://dx.doi.org/10.1109/TIT.1962.1057692, Conference Name: IRE Transactions on Information Theory.

[47] J. Reddaway, P.E. Richardson, R.J. Bevan, J. Stoneman, M. Palombo, Microglial morphometric analysis: so many options, so little consistency, Front. Neuroinformatics 17 (2023) http://dx.doi.org/10.3389/fninf.2023.1211188, Publisher: Frontiers.

[48] R.L. Graham, F. Frances Yao, Finding the convex hull of a simple polygon, J. Algorithms 4 (4) (1983) 324–331, http://dx.doi.org/10.1016/0196-6774(83)90013-5.

[49] A. Barragán-Montero, U. Javaid, G. Valdés, D. Nguyen, P. Desbordes, B. Macq, S. Willems, L. Vandewinckele, M. Holmström, F. Löfman, S. Michiels, K. Souris, E. Sterpin, J.A. Lee, Artificial intelligence and machine learning for medical imaging: A technology review, Phys. Medica: Eur. J. Med. Phys. 83 (2021) 242–256, http://dx.doi.org/10.1016/j.ejmp.2021.04.016, Publisher: Elsevier.

[50] H. Zerouaoui, A. Idri, Reviewing machine learning and image processing based decision-making systems for breast cancer imaging, J. Med. Syst. 45 (1) (2021) 8, http://dx.doi.org/10.1007/s10916-020-01689-1.

[51] M.R. Damani, L. Zhao, A.M. Fontainhas, J. Amaral, R.N. Fariss, W.T. Wong, Age-related alterations in the dynamic behavior of microglia, Aging Cell 10 (2) (2011) 263–276, http://dx.doi.org/10.1111/j.1474-9726.2010.00660.x, _eprint: https://onlinelibrary.wiley.com/doi/pdf/10.1111/j.1474-9726.2010.00660.x.

[52] C. Nuñez-Diaz, E. Andersson, N. Schultz, D. Pocevičiūtė, O. Hansson, K.P.R. Nilsson, M. Wennström, The Netherlands Brain Bank, The fluorescent ligand bTVBT2 reveals increased p-tau uptake by retinal microglia in Alzheimer's disease patients and AppNL-F/NL-F mice, Alzheimer' s Res. Ther. 16 (1) (2024) 4, http://dx.doi.org/10.1186/s13195-023-01375-7.